Powder Aerosol Deposition and Polymers: Is There Hope for a Common Future?

Marc Christopher Thiel and Karen Lienkamp*

Polymer–ceramic composites (PCCs) are promising functional materials with applications in energy technology, microelectronics, sensor technology, protective coatings, wastewater treatment or for biomedical purposes. Unfortunately, ceramics require high-temperature sintering, while polymers only have a limited thermal stability. Therefore, PCC fabrication is quite complex and requires strict process control. This severely limits the efficiency and economy of the process and the reproducibility of the desired materials properties. Powder aerosol deposition (PAD) is a spray-coating process in which ceramic powders are accelerated by a pressure difference using a carrier gas. They are then deposited as nanocrystalline, dense coatings onto a substrate without the need for additional sintering. In the current PAD research, the focus is ceramic powders. Yet there are also examples of polymer and ceramic particles that have been codeposited. Much of this works is trial-and-error, and a general concept for deposition of PCCs by PAD is not yet available. This review revisits the fundamentals of PAD and the most important process parameters that were studied experimentally and in silico. It connects these with recent work on the combination of polymers and ceramics in the PAD process to highlight and evaluate the future of this field from a polymer science perspective.

1. Introduction

Powder aerosol deposition (PAD), also called vacuum kinetic spray, vacuum cold spray, or simply aerosol deposition (AD), is a thermal spray method that was originally designed to obtain sinter-free, highly dense, and thin ceramic layers at room temperature. The term AD was first used in the late 1990s by Akedo et al. at the Agency of Industrial Science and Technology in Japan, whose team deposited and characterized lead zirconate titanate (PZT) films on silicon substrates.[1] Since then, AD technology spread throughout the world,[2] with research being conducted primarily in South Korea,[3–5] Japan,[6–8] the United States of America,[9,10] and Germany.[11–13] Today, PAD research is still confined to a small number of research groups working on mechanistic studies,[14–16] in some cases combined with simulation methods,[13] on process parameter studies,[17–20] on process setup modifications,[21,22] or on the development of new types of materials with unique architectures that are not easily accessible by other processes. Examples for the latter are solar cells with a dry-processed perovskite absorber layer,[23] flexible thermoelectric generators,[24] or multilayered materials such as metal–ceramics composites.[25]

One of the advantages of the process is that a wide range of powder types can be used, which makes new materials combinations possible. In a process variation called aerosol co-deposition (AcD), powder mixtures of two or more materials are used.[2] AcD yields composite films made from different ceramic powders,[26] from mixtures of metals and ceramics[27] or polymer–ceramic composites (PCCs).[28]

We here review the fundamentals of the PAD process, first focusing on experimental works concerning the deposition mechanism, the most important process parameters and their influence on the process. This is followed by a summary of crucial in silico work that confirms and adds further details to the experimental findings. Finally, work dealing with the combination of ceramics and polymers in the PAD process is presented and discussed.

2. Basics of PAD

2.1. The PAD Device and Operating Principle

In PAD, fine particles with a size range of 0.08–2 μm[29] are accelerated to velocities of up to several $100\,\mathrm{m\,s^{-1}}$ by a carrier gas and guided toward a static or moving substrate. When the particles collide with the substrate, they fracture into nanometer-sized pieces that are then deposited as a dense, adhesive film with a nanocrystalline microstructure. The film formation takes place at room temperature, yet the temperatures during collision are significantly higher (up to 500 °C). For a substrate size of

M. C. Thiel, K. Lienkamp
Professur für Polymerwerkstoffe
Fachrichtung Materialwissenschaft und Werkstofftechnik
Universität des Saarlandes
Campus C4.2, 66123 Saarbrücken, Germany
E-mail: karen.lienkamp@uni-saarland.de

The ORCID identification number(s) for the author(s) of this article can be found under https://doi.org/10.1002/adem.202400503.

a few cm^2 up to 1000 cm^2, a film thickness of several micrometers can be obtained in a few minutes.

A typical PAD setup is shown in **Figure 1**a. It consists of an aerosol chamber in which a fine aerosol is generated from a powder, and a deposition chamber where the substrate is located. Both chambers are connected by a feedthrough that has a nozzle at the end. The operating pressure of the aerosol unit is typically between 60 and 1066 mbar,[2] while the deposition chamber is kept at a pressure of 0.2–20 mbar by a strong vacuum pump. The aerosol chamber is located on a vibrating table, and the powder particles are aerosolized by these vibrations.

When a carrier gas is introduced into the aerosol chamber, an aerosol jet forms because of the pressure difference between the two chambers. The airborne powder particles are accelerated by this jet into the deposition chamber and onto the substrate.[2] The substrate is moved laterally at a defined speed using an x–y stage, thereby defining the size of the area that is coated with the dense nanocrystalline film.

Figure 1b summarizes the unique properties of the PAD process and the deposited films. One of the most important properties of the PAD process is that it yields dense ceramic layers without additional sintering at high temperatures, making new material combinations (e.g., ceramic/metal, ceramic/polymer) easily accessible.[30] In addition, the film growth rate is high (5–50 µm min^{-1}) compared to many other film-forming processes.[31] Further, a nanocrystalline ceramic microstructure is created, which is difficult to obtain with other methods (e.g., pressureless sintering, hot pressing, etc.).[32]

2.2. Deposition Mechanism of PAD

In previous reviews, Akedo described the PAD process as follows:[29,33,34] ceramic particles with a size range of 0.08–2 µm are accelerated through a nozzle up to speeds of several hundred meters per second using a carrier gas. They impact the substrate, where a part of their kinetic energy is converted into bonding energy. This results in strong adhesion between the substrate and the particles, and between the particles themselves.[29,34] The mechanism by which this energy conversion takes place is not fully understood,[29,33,34] but since a reduction in crystallite size and a deformation of the impinging particles is observed in the deposited films,[33] the phenomenon is described as room-temperature impact consolidation (RTIC).[29,33,34] Hanft et al. previously discussed the deposition mechanism of PAD in detail.[2] In this work and other publications, the following experimental findings that give insight into the PAD mechanism have been highlighted as follows.

1) In PAD process finite-element simulations, the temperature at the impact site increased, but remained far below the sintering and melting temperatures of ceramics. The simulations showed that the energy transmitted by the impact was of the same order of magnitude as the fracture strength of typical ceramics.[29,33,34] This explains why particles fracture into nanoscale pieces during PAD.

2) Deposition of ceramic particles of a suitable size range takes place via fragmentation and/or plastic deformation (RTIC mechanism). Smaller particles follow the gas flow (bow shock deflection) or bounce off elastically, while larger particles cause abrasion.[2,29,34] While ceramics usually undergo brittle fracture under mechanical stress, the occurrence of plastic deformation of the ceramic particles in PAD was proven in several experiments and is a size-dependent brittle-to-ductile transition, which occurs at room temperature under the high-pressure load of the impact.[34]

3) There is a "deposition window" in which successful particle deposition occurs which depends on the particle velocity (ν),[2] as illustrated in **Figure 2**a. ν is mainly determined by the carrier gas
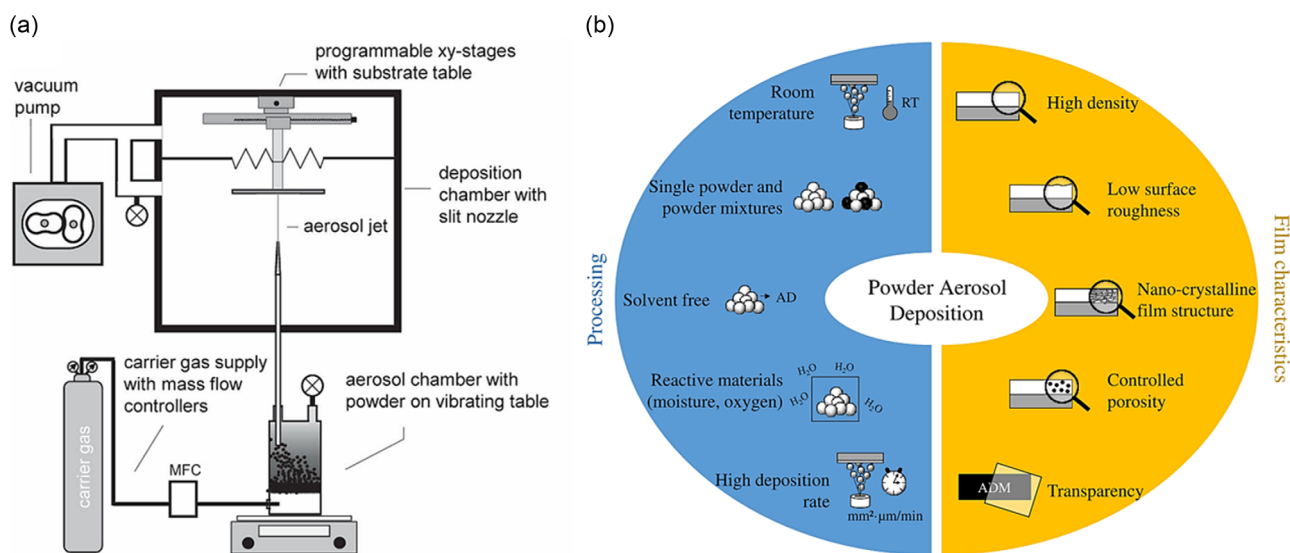

Figure 1. The PAD setup, characteristic features of the process and the materials obtained. a) The setup consists of an aerosol generation unit and a deposition chamber containing the substrate. These are connected via a feedthrough that ends with a nozzle. The aerosolized particles are accelerated onto the substrate by a pressure difference between the two chambers using a carrier gas and deposited on the substrate. Reproduced with permission.[2] Copyright 2015, Göller Verlag GmbH. b) Summary of important features of the PAD proces, and of the materials properties obtained by PAD. Reproduced with permission.[30] Copyright 2019, World Scientific Publishing Company.
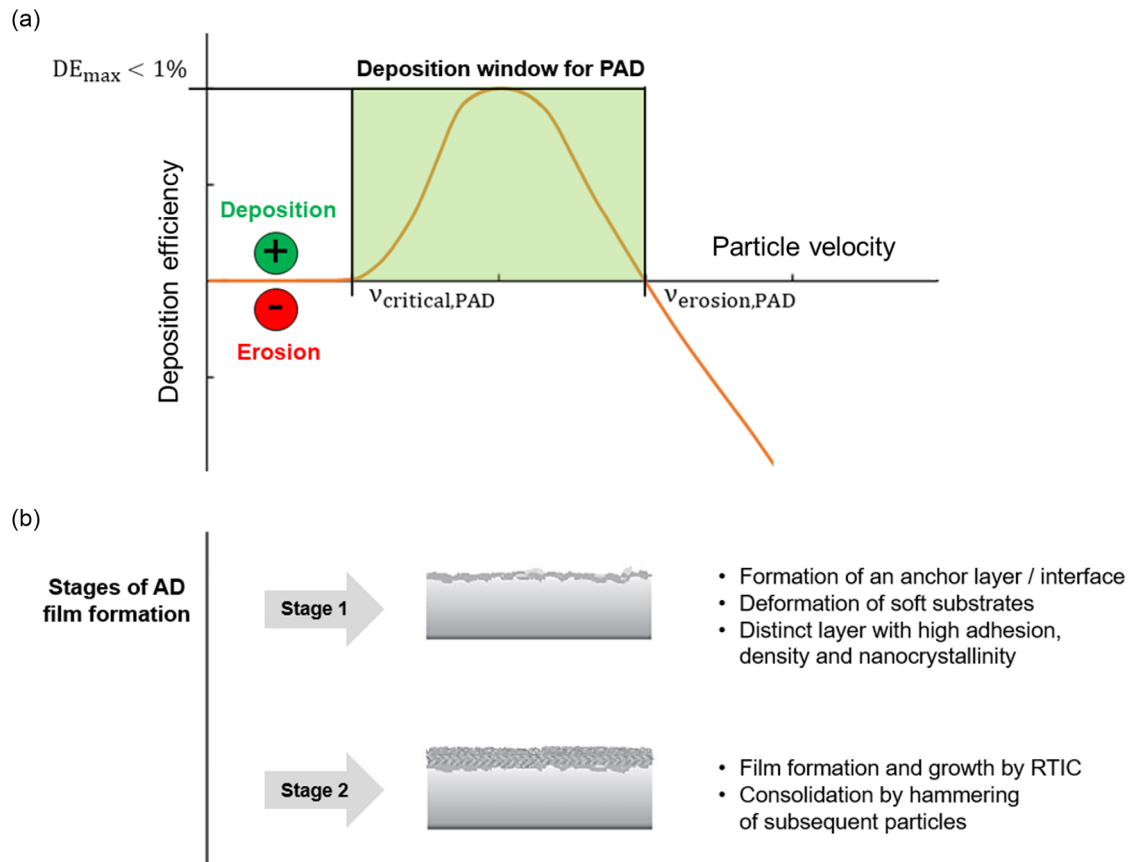
**ADVANCED
SCIENCE NEWS**

www.advancedsciencenews.com

**ADVANCED
ENGINEERING
MATERIALS**

www.aem-journal.com

(a)

(b)

Figure 2. Deposition window and stages of PAD. a) Deposition of a PAD film is possible at particle velocities above the first critical particle velocity, $\nu_{\text{critical,PAD}}$, and below the second critical particle velocity, $\nu_{\text{erosion,PAD}}$. Above $\nu_{\text{erosion,PAD}}$, erosion of the substrate takes place. Within the deposition window, the deposition efficiency (DE) can reach a maximum value, which is usually below 1 wt% of the injected material for ceramic powders. b) After formation of a strongly adhesive and dense anchor layer (Stage 1), the film grows and consolidates by a hammering effect where incoming particles mechanically impact the layers underneath (Stage 2). Adapted with permission.[2] Copyright 2015, Göller Verlag GmbH.

flow rate.[29,33] For a suitable powder, deposition is possible if $\nu > \nu_{\text{critical,PAD}}$, while no deposition takes place below this critical velocity. At $\nu > \nu_{\text{erosion,PAD}}$, erosion of the substrate occurs.[2] The deposition efficiency (DE) can reach a maximum within this deposition window.[2] DE can be defined according to Equation (1):[35]

$$DE = \frac{m_{\text{f}}}{m_{\text{p,0}} - m_{\text{p,1}}} \cdot 100\% \qquad (1)$$

where m_{f} is the mass of the deposited film (calculated from the film thickness, the coated area, and the density of the deposited material), and $m_{\text{p,0}}$ is the powder mass in the aerosol chamber before deposition and $m_{\text{p,1}}$ after the deposition.[35]

4) The critical velocity of a certain powder also depends on the material type of both the particles and the substrate. For example, a critical velocity of 150 m s^{-1} was observed for α-Al$_2$O$_3$ and PZT ceramics deposited on silica glass (measured using a time-of-flight method).[33] Other groups derived the particle speed from the gas flow rate of the carrier gas. For example, $\nu_{\text{critical,PAD}}$ calculated from the gas flow rate was 2 L min^{-1} for an Fe-based amorphous alloy on soda-lime glass[36] and 5 L min^{-1} for yttria-stabilized zirconia (YSZ) on a Cu substrate.[37]

5) Based on findings for the PAD of Al$_2$O$_3$–PZT composite powder on silica glass substrates,[33] Al$_2$O$_3$ on Cu,[3] on Al$_2$O$_3$,[38] and on soda-lime glass substrates,[39] Ti$_3$SiC$_2$ on glass substrates,[40] Al$_2$O$_3$–Ag composite powder on Al substrates,[41] and mullite on Si substrates,[42] it is assumed that the PAD mechanism is a two-stage process. First, an anchor layer is formed which provides adhesion to the substrate. Second, the deposited layer densifies and grows in thickness via the RTIC mechanism (Figure 2b).[2]

6) Reactive surfaces are formed when the particles fragment into nanoscale pieces. Reactions of these surfaces enable adhesion to the substrate and the formation of a nanocrystalline microstructure.[34]

From the earlier-listed mechanistic features, (1)–(4) are consensus in the relevant literature, while (5) and (6) are still under debate. It is still an open question whether an anchor layer really forms as the first step, and if so, if this is the case for all systems, and what the exact features of such an anchor layer are. In their first PAD paper, Akedo et al. observed a "damage layer" of 100–150 nm thickness when investigating the cross section of a Si substrate coated with PZT by transmission electron microscopy (TEM) (**Figure 3**a).[1] The damaged Si surface had stacking
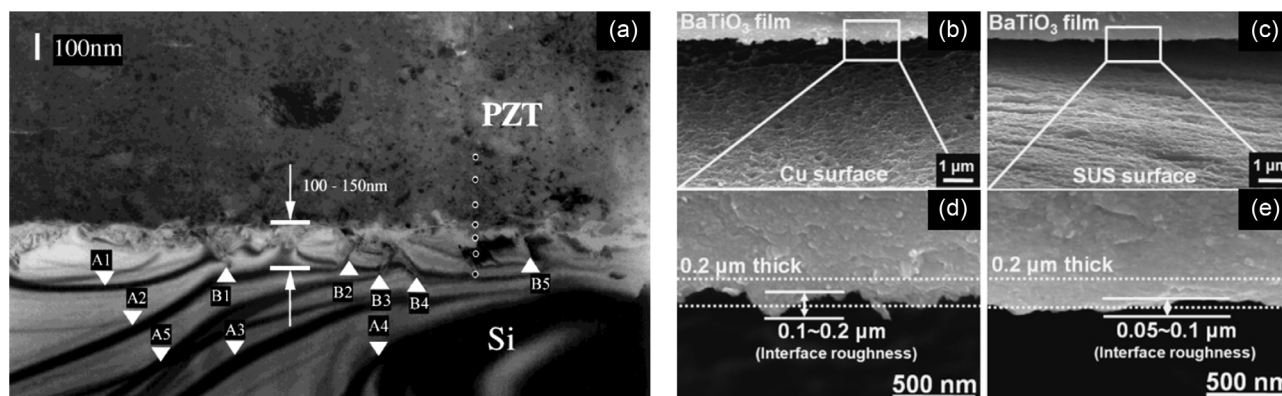
Figure 3. Images of different damage layers. a) TEM cross section of a Si substrate coated with PZT, showing deformations in the substrate (A1–A5) induced by stacking faults (B1–B2). Reproduced with permission.[1] Copyright 1999, The Japan Society of Applied Physics, IOP Publishing. b–e) Interface roughness of (b,d) Cu substrates and (c,e) stainless-steel substrates, both coated with BaTiO$_3$. The roughness of the softer Cu substrate is higher than that of the stainless-steel substrate. Reproduced with permission.[43] Copyright 2009, The Japan Society of Applied Physics.

faults (B1–B5 in Figure 3a), which induced deformations in the Si wafer (A1–A5 in Figure 3a). Later papers confirmed the existence of a deformed interface between the film and substrate after successful PAD.[3,17,35,37,43–50] These data suggest that initial deformation of the substrate surface by the particles is crucial for the formation of an anchor layer. Oh and Nam compared cross sections of BaTiO$_3$ films deposited on Cu and stainless-steel substrates. They showed that a higher interfacial roughness was obtained for the softer Cu substrates than for the harder stainless-steel substrates (Figure 3b–e).[43] A correlation between a higher substrate ductility and a higher interfacial roughness was also found for Al$_2$O$_3$ on Cu, Al, and stainless-steel substrates[17,45,48,50]; for Y$_2$O$_3$ on Sn, Al, stainless steel, and bulk metallic glass (BMG) substrates[46]; for Al$_2$O$_3$ on glass substrates; and for glass on glass and stainless-steel substrates.[17] Interestingly, when very hard substrates such as Al$_2$O$_3$ and sapphire were used, no significant deformation was observed, yet films with sufficiently strong adhesion were still obtained.[17,30,50]

These findings indicate that the morphology and properties of the interface between the substrate and the deposited film is affected by the mechanical properties of the substrate, and is most likely related to the magnitude of its hardness relative to the impact energy of the particles. The anchoring layer thus could be considered as a deformation-rich layer within the substrate directly adjacent to the substrate-coating interface that forms when softer substrates are used, but that is not prerequisite for sufficient adhesion of the deposited film. There are also indications that the fragmentation of the particles at the interface changes with very soft substrates such as polymers.[51] In this case, not only a deformed substrate is detectable, but the directly adjacent PAD layer also exhibits a microstructure that differs from the subsequent layers,[51] which will be discussed in detail later. Thus, depending on the material combination of particles and substrate used, the definition of the anchor layer could also be extended to include the microstructure of the film directly at the interface.

Lee et al. investigated the anchor layer formation in more detail using Al$_2$O$_3$ particles deposited on soft copper and glass substrates, as well as on hard Al$_2$O$_3$ and sapphire substrates.[44]

After depositing one layer of particles on glass and sapphire as model systems by a single scan, they treated the substrates with ultrasound and thereby removed unbound particles. When imaging these surfaces with scanning electron microscopy (SEM) before ultrasonic cleaning, plastically deformed (flattened) and bonded Al$_2$O$_3$ particles were found on the plastically deformed glass substrate. In the case of the hard sapphire substrate, broken unbound particles were observed. After cleaning, the deformed bonded particles remained on the deformed glass substrate, while all particles were removed from the undeformed sapphire substrate. For copper substrates, the results were similar to those obtained for the glass substrate.[3] When several scans were performed on all substrates, an immediate onset of film formation was observed for the soft copper and glass substrates, while film formation for the hard Al$_2$O$_3$ and sapphire substrates started with a time delay, which the authors associated with more difficult anchor layer formation.[44] With an increase of the particle impact velocity by increasing the carrier gas consumption from 5 to 7 L min^{-1}, the hard sapphire substrate was etched by the particles without film formation.[44] This work shows that a deformed anchor layer is only formed in systems with sufficient energy for a plastic deformation of the substrate. When the surface deformation energy is higher than the kinetic energy of the particles (which is still sufficient to fracture and deform the particles) as in the case of Al$_2$O$_3$ particles on the sapphire substrate, the fractured particles remain unbound. Additionally, the work demonstrated that the layer formation on hard substrates does not only dependent on the particle kinetic energy, but also on the deposition time. The study, while otherwise very insightful, did not investigate the time-dependent changes on the surface in detail (e.g., any indications of an anchor layer formation), or the morphology obtained at the onset of film formation on the sapphire substrate. Schubert et al. also reported cases of hard substrates (sapphire, Al$_2$O$_3$) where classical anchor layers as described earlier were absent, but the deposited films still adhered.[31] In these cases, there must be different origins to the adhesion of the coating.

The microstructure of the substrate–film interface of Al$_2$O$_3$ particles on copper, stainless steel, and aluminum was also
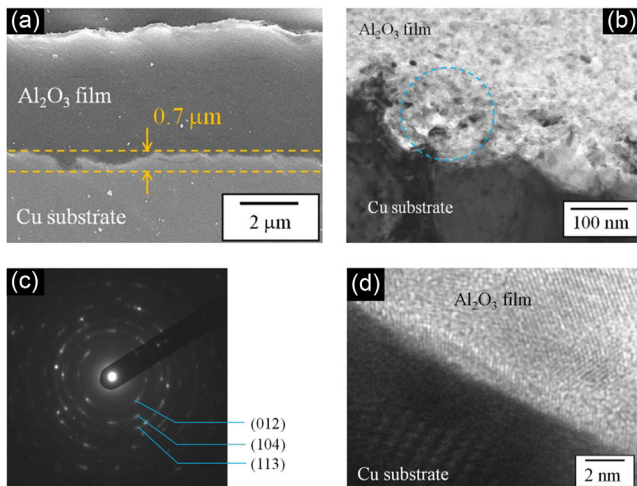
Figure 4. Interface between a PAD film and a substrate on different length scales. a) The SEM cross section of a Cu substrate coated with Al_2O_3 shows a deformed layer with a roughness of about 0.7 μm. b) The bright-field TEM cross section of the same material reveals dark areas in the Al_2O_3 PAD film. c) The selected area diffraction pattern measured in the blue circle in (b) shows diffraction spots corresponding to randomly oriented Al_2O_3 crystallites. d) HR-TEM imaging shows a smooth Al_2O_3/Cu interface, which indicates the absence of mechanical interlocking at the atomic level. Adapted with permission.[45] Copyright 2014, ASM International.

studied by high-resolution TEM (HR-TEM).[45,48] While deformation was observed for higher length scales (100 s of nm to μm) for these substrates, no distinct interfacial layer was observed at lower length scales (10 s of nm), as shown in **Figure 4** for a Cu substrate: at large length scales, a surface roughness of 0.7 μm was estimated (Figure 4b). A selected area diffraction pattern (SADP) measured in the blue-circled region in Figure 4b contained only diffraction spots corresponding to randomly oriented Al_2O_3 crystallites (Figure 4c). This showed that the bright-dark contrast in that area in Figure 4b originated from a nonuniform thickness of the sample and not from a different

chemical composition. At a length scale of tens of nanometers, the interface was uniform (Figure 4d).[45] Similar results were found for Al and stainless-steel substrates.[48] Naoe et al. further investigated the interface chemistry using scanning TEM electron energy-loss spectroscopy (STEM–EELS) (**Figure 5**).[45] Point 5 in the high-angle annular dark field (HAADF)–STEM image (Figure 5a) is in the same area in which the SADP in Figure 4c was recorded. Chemical mapping by EELS along that interface showed a main peak at 537 eV corresponding to O–K edge and a low-intensity peak of a Cu–O signal, which was exclusively found at one measurement point along the interface. This was interpreted as confirmation of a chemical bond forming between the substrate and the particles. From the presented data, it is difficult to assess if this peak is significant and can be reproducibly found within the Cu/Al_2O_3 interphase, or if it is a locally unique observation.

Taken together, the SEM/TEM cross sections and EELS spectra were interpreted as evidence that the interaction of the colliding particles and the substrate is not a purely physical process that leads to mechanical interlocking (i.e., a classical anchoring effect), but that in addition, chemical interactions contribute to film adhesion, especially in the case of the hard substrates. Additional diffusion processes, e.g., lateral diffusion of atoms on the surface as observed during conventional sintering could be excluded since the temperature at the interface is too low for such processes.

Akedo et al. provided an experiment that justifies the assumption of chemical bonds forming between the particles and the substrate (**Figure 6**).[34] In the two-substrate setup used, an Al_2O_3 substrate (obtained by sintering the same type of Al_2O_3 powder that was also used for their PAD process) and a glass substrate were mounted orthogonally to each other. Al_2O_3 particles that were unsuitable for a conventional PAD process due to a too large particle size were intentionally used. As expected, when these particles collided with the Al_2O_3 substrate, its surface was etched, while the particles themselves fractured. Some of the fractured particles were then reflected with less than the critical velocity for RTIC onto the glass substrate mounted at a 20 cm distance. On that substrate, an adhesive, low-density film of 1 μm
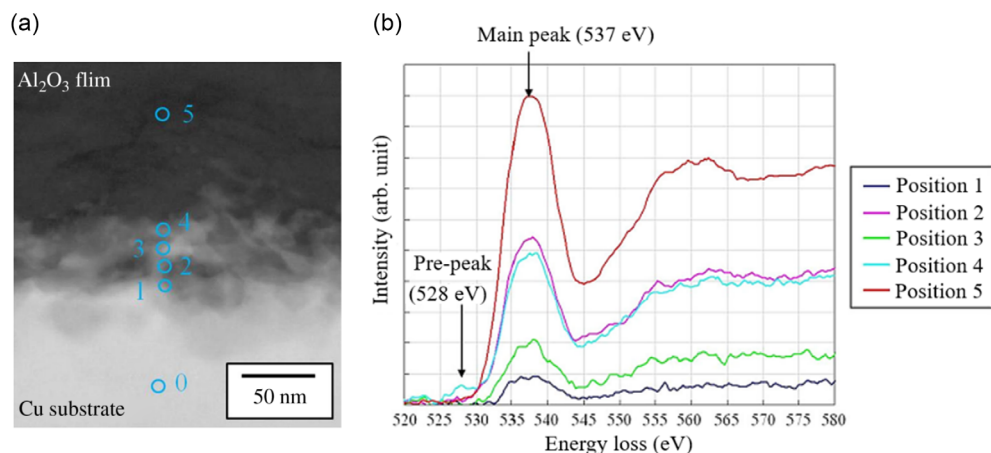
Figure 5. Investigation of the binding state at a Cu/Al_2O_3 PAD interface via STEM–EELS. a) HAADF–STEM cross section of Cu substrate coated with Al_2O_3 with measurement points for EELS. b) EELS spectra near the O–K edge (main peak) for five measurement points: At position 4, a pre-peak was observed at 528 eV, which was assigned to a Cu–O chemical interaction. Adapted with permission.[45] Copyright 2014, ASM International.
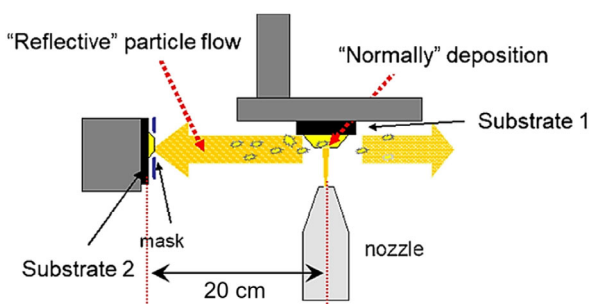
**ADVANCED
SCIENCE NEWS**

www.advancedsciencenews.com

**ADVANCED
ENGINEERING
MATERIALS**

www.aem-journal.com

Figure 6. Two-substrate setup used to study the PAD deposition mechanism by reflection deposition. Two substrates were mounted orthogonally to each other. Substrate 1 was etched away by the large Al_2O_3 particles used, while the broken particles were reflected onto substrate 2. A PAD film formed on substrate 2, which indicates that the binding takes place via fresh reactive surfaces. Adapted with permission.[34] Copyright 2020, Japan Science and Technology Agency.

thickness formed, even though the fractured particles did not have sufficient kinetic energy for the conventional RTIC mechanism.[34] It is known, e.g., from the field of mechanochemistry, that freshly fractured surfaces can exhibit a marked chemical reactivity due to unsaturated chemical bonds.[52] Delogu, for example, indirectly demonstrated the chemical reactivity of fractured particles by grinding α-quartz powder in ethanol in the presence of the free radical 2,2-diphenyl-1-picrylhydrazyl (DPPH).[53] Fracturing of the quartz particles led to the formation of radicals at the particle surface, which subsequently reacted with ethanol and formed a hydrogen radical. That hydrogen radical was able to react with DPPH. With increasing grinding time, the concentration of DPPH was reduced, while the specific surface area of the powder increased due to the size reduction of the particles. This can be seen as indirect evidence for the chemical reactivity of the freshly formed surfaces.[53] For the PAD process, this means that the particle fragments would require the substrate surface to also have an increased chemical reactivity for efficient initial anchoring. In the above-described PAD experiment, it was assumed that particles hitting the glass surface during the initial phase of the experiment removed contaminations from the substrate, similar to sandblasting,[29] and thereby created a fresh reactive substrate surface that could interact with the fractured particles. Thus, adhesion between the particles and the surface would be due to chemical bonding, not due to a physical impact. Khansur et al. showed via contact angle measurements that the surface energies of different substrates changed after PAD and subsequent dissolution of the deposited NaCl films.[49] This could indicate a change in the reactivity of the substrate surface after impact, although there are also other explanations for these findings (e.g., changes in the surface roughness).

For both covalent and ionic bonding, a change in the electron distribution between participating atoms is required. It is known that high-energy fracture processes can cause electric discharges, a phenomenon called fracto-emission.[54,55] Evidence for fracto-emission during PAD was provided by Akedo et al.[56] When monitoring the optical emission spectra of helium used as carrier gas for the deposition of PZT on a quartz plate with an optical fiber and a time-resolved spectrometer, sharp emission lines were observed. These lines coincided with the He spectrum lines induced by electric discharge.[56] In a recent paper, Lee et al. used a PAD setup similar to the two-substrate setup in Figure 6, but with additional electrodes. This allowed influencing the flight path of the particles reflected onto the second substrate by applying an orthogonal electric field (**Figure 7**).[16] In the absence of the field, the secondary particles produced by fracture on the first substrate impacted the second substrate and formed a dense film. When an electric bias of +250 V was applied between the electrodes, a porous film with a larger crystallite size than in the absence of the electric field formed. At the same time, many secondary particles were deposited on the grounded electrode. This indicated that the secondary particles formed during the PAD process were mostly positively charged. In ab initio calculations, a correlation between a positive charge of the particles and facilitated plastic deformation due to a reduced generalized stacking fault energy was observed.[16]

To summarize, parts of the RTIC mechanism propagated by Akedo, for example, the fracture and deformation of particles after impact on the substrate surface, are understood and have been confirmed for a large number of systems. In contrast, while there is solid evidence for the formation of an anchoring layer in many systems, it is absent in others, and in these cases, the origin of particle adhesion on the substrate is still unclear. Thus, an accepted general theory for the binding of a PAD film onto substrate surfaces is still lacking. Future work could focus on finding uniform, quantifiable criteria for anchor layer formation, and on investigations of the bonding state at the interface between a PAD film and the substrate surface—especially in those cases where an anchor layer is absent. Atom probe microscopy and tomography may become helpful tools in such studies.

2.3. Parameters Influencing PAD Processes

Several characteristics of the experimental setup and the powder used influence the PAD process and the properties of the layers obtained. Many authors studied the effects of varying the powder characteristics (i.e., crystallite size, particle size, and morphology), the powder pretreatment (i.e., sieving, drying, preheating, and milling),[48,57–67] the process parameters (i.e., mode of aerosol generation,[58,68] carrier gas type and carrier gas flow rate,[11,19,35–37,69–71] nozzle type and the evolution of the gas flow field,[19,35,37,44] deposition angle[72]), as well as characteristics of the substrate (i.e., roughness, hardness, and substrate temperature).[31,44,73,74]

2.3.1. Influence of Powder Characteristics and Pretreatment

The first step for a successful PAD process is the preparation of a suitable powder. Exner et al. suggested three criteria for such powders[66]: First, the particle size should be in the submicron to low micron range. Second, the powder particles should have a low specific surface area. Third, the powders should be moisture free. In addition to suitable particle sizes, a minimum crystallite size apparently also plays a decisive role.[66] As only a small number of commercially available powders fulfill these criteria, establishing a suitable powder preparation routine is essential for
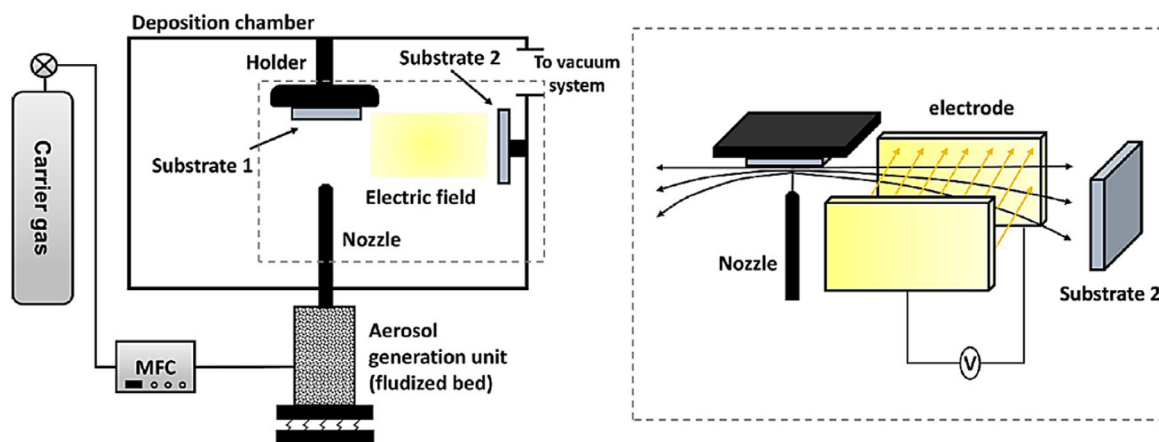
Figure 7. Influence of an electric field on reflection deposition. The morphology of a PAD film formed on substrate 2 changed from dense to porous when an electric field of $+250$ V was applied between the electrodes, while at the same time, a large number of secondary particles were deposited on the grounded electrode. This indicated that secondary particles created during PAD are mostly positively charged due to fracto-emission. Reproduced with permission.[16] Copyright 2023, American Chemical Society.

a PAD lab. One of the first papers on powder preparation was presented by Lebedev et al.[57] Using the PAD of PZT powder on glass and stainless-steel substrates as model system, they investigated the effect of dry ball milling and powder preheating on the deposition rate, microstructure, and electric properties of the coatings obtained. It was found that pretreating the powder by ball milling for 5 h at a rotation speed of 200 rpm increased the powder deposition rate by up to a factor of 30, while heat treatment at 800 °C decreased the deposition rate and simultaneously improved the electric properties of the obtained layers.[57] Mihara et al. studied a wider range of powder preparation parameters including sieving, drying, heating, and ball milling in different combinations.[58,59] At fixed deposition conditions, previous sieving and drying increased the obtained layer thickness compared to the untreated powder because these processes reduce the number and size of large agglomerates. Dry ball milling for 1 h with a rotation speed of 200 rpm increased the film thickness most significantly, because it not only reduced the agglomerates, but also crushed larger particles into smaller ones. As previously observed, heat treatment up to 800 °C without additional ball milling also reduced the film thickness in these studies.[58,59] This has been linked to increased particle sintering, which increased the size of the agglomerates and the interaction force between the primary particles. It was found that there is an optimal size of agglomerates that increases the deposition rate. Agglomerates that are too large are more difficult to aerosolize, while smaller agglomerates do not have sufficient kinetic energy for successful deposition. Aggregates with too strong interparticle adhesion consume much of their kinetic energy for breaking during impact instead of undergoing deformation and contributing to film formation.[58,59] The influence of the agglomeration state was confirmed by Fuchita et al.[61] They tested eleven different zirconia powders with different particle sizes and specific surface areas. They reported that for their system, a highly dense film formed only for powders with a particle size between 2.1 and 3.5 μm and a specific surface area in the range of 4.4–6.5 $m^2 g^{-1}$. They concluded that the agglomeration state of the primary

particles was the determining factor for successful film formation, as agglomeration affects the specific surface area of the powders.[61] In a very detailed study, Exner et al. investigated the effect of particle size, specific surface area, and compressibility index on the PAD success using fourteen different α-alumina powders combined with substrates of different hardness.[65] They found for the harder substrates that powders with surface areas from 5.5 to 8 $m^2 g^{-1}$, a high compressibility index, and only loosely agglomerated particles in the range of a few hundred nanometers in diameter had the highest deposition rates. For the softer substrates, larger particles in the range of 1.5–4.5 μm with a lower specific surface area and a compressibility index of 44–47% were more successful.[65]

Exner et al. also studied the effect of powder pretreatment using commercial ceria powders with an average particle diameter of 15–30 nm, which was well below the previously reported suitable range for PAD.[66] The powders were heated at typical sintering temperatures from 900 to 1400 °C (44–63% of the melting temperature of ceria) for 10 h to induce aggregation, followed by ball-milling treatment and sieving to adjust the agglomerate size. It was shown that a dense, well-adhering film was only formed when a certain minimum crystallite size was exceeded during heat treatment. Above that critical value, the actual particle size was not important. Furthermore, the crystallite size in the deposited film was significantly smaller than that of the pretreated powder, which can be considered as a confirmation of the RTIC mechanism.[66] These findings were confirmed by Hanft et al. using tin oxide nanoparticles.[67]

In recent work, the conventional AD system was extended with an in-line powder production unit. This upstream unit could be used for ultrasonic spray pyrolysis (USP),[75,76] as shown in **Figure 8**a. In USP, droplets of a precursor salt solution are fed into a high-temperature furnace reactor via a nebulizer in which the solvent evaporates and the remaining salt particles oxidize.[76] This leads to a defined particle size distribution which can be controlled via the operating parameters of the reactor and the nebulizer.[76] For example, Ghosh et al. used tin (II) and Song
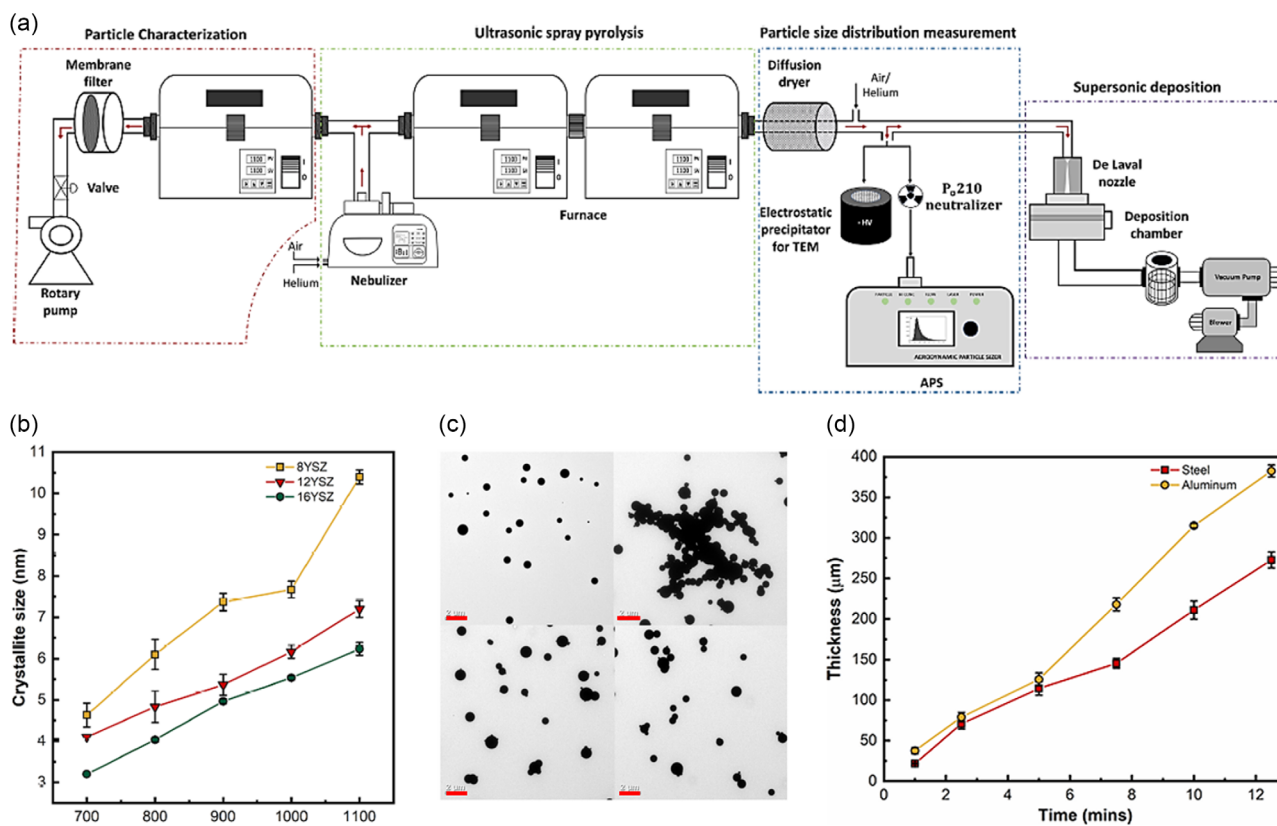
Figure 8. USP–AD setup and deposition characteristics. a) Scheme of a USP–AD unit. b) Crystallite size of different YSZ particles (named 8YSZ, 12YSZ, and 16YSZ) as a function of the furnace working temperature. c) Images of 8YSZ particles prepared at a furnace working temperature of 1000 °C (scale bars = 2 µm). d) Film thickness evolution of layers obtained with 12YSZ on steel and aluminum substrates. Adapted with permission.[76] Copyright 2021, Wiley-VCH GmbH.

et al. dissolved zirconium (IV) oxynitrate hydrate and yttrium (III) nitrate hexahydrate in various ratios in water to obtain YSZ particles with 8, 12, and 16 mol% yttria.[75,76] To analyze the USP products, Song et al. fed the precursor droplets into a tube furnace operating at different temperatures between 700 and 1100 °C and then deposited them on a glass fiber filter (left side in Figure 8a), so that they could be imaged by TEM or characterized using an aerodynamic particle sizer.[76] For the PAD process, the particles were passed through a furnace with a working temperature of 1000 °C and a subsequent diffusion dryer, where the relative humidity of the powder was adjusted to 75% (right side in Figure 8a) before entering the deposition chamber.[76] The crystallites of the particles increased with increasing furnace temperature (Figure 8b). Very uniformly distributed particles sizes were obtained for a furnace temperature of 1000 °C (Figure 8c).[76] Dense nanocrystalline films were produced for both SnO_2 and YSZ using this method.[75,76] This modification of the PAD process has several advantages on different levels. First, the chemical composition of the precursor could be changed in situ, which in a conventional process would involve a series of powder preparation steps (grinding, drying, sieving, heat treatment); second, the particle size and degree of crystallinity could also be adjusted, making it easier to optimize process parameters and thus possibly improve the DE. In addition, a

closed process excluded impurities resulting from a multistage powder preparation routine (e.g., due to abrasion of the grinding tools during ball milling). As a further advantage, the particles were aerosolized from the beginning. As explained in more detail later, in the conventional process, the powder is aerosolized via a fluidized bed, which means that not all particles in a powder are aerosol compatible and that the aerosol is depleted of particles suitable for the PAD process overtime. This is not the case with the PAD process combined with USP. One disadvantage that must be considered, however, is that the flexibility for using mixed powders is limited. Additionally, the process is not compatible with polymer particles due to the high temperatures used.

2.3.2. Influence of Aerosol Generation and Carrier Gas Type

After a suitable powder pretreatment, the next challenge in PAD is to successfully aerosolize the powder, an aspect of PAD which has not yet been studied in a much detail. The commonly used aerosol unit is a fluidized bed generator (**Figure 9**a).[68] In this setup, the powder particles are aerosolized by vibration while flushing the aerosol chamber with the carrier gas. Hanft et al. compared this setup with a commercial aerosol generator in which the powder is fed from a reservoir via a piston into a rotating brush, where it is aerosolized by blowing the particles off the
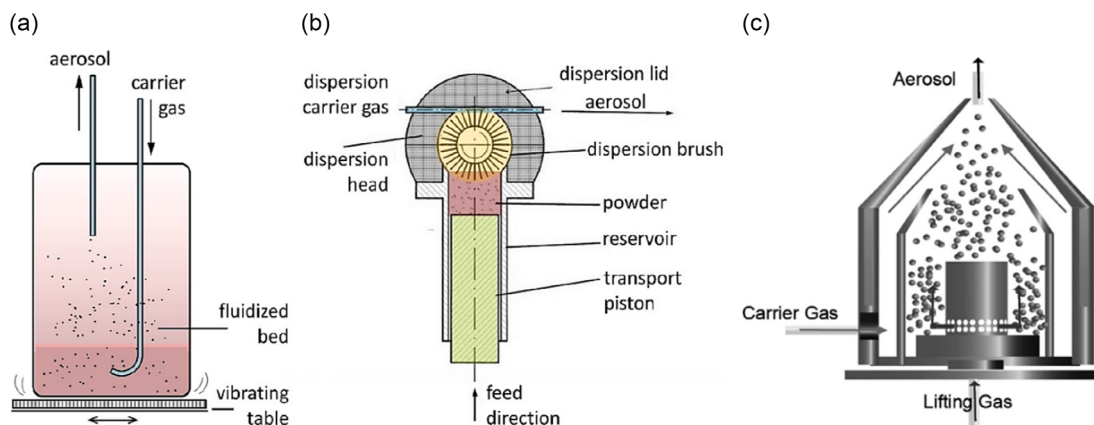
Figure 9. Three different aerosol generation units. a) In a fluidized bed generator, powder is aerosolized by vibrations and transported into the deposition chamber using the carrier gas. b) In a commercial powder dispersion unit, a piston transports the powder from the reservoir to a rotating brush, where it is blown off the bristles by the carrier gas. Reproduced with permission.[68] Copyright 2015, Göller Verlag GmbH. c) In the modified aerosol generation unit from Mihara et al., the powder is aerosolized by a lifting gas and transported into the deposition chamber by the carrier gas. Reproduced with permission.[58] Copyright 2009, Japan Science and Technology Agency.

bristles with the carrier gas.[68] In the fluidized bed generator, the small particles and agglomerates are aerosolized and deposited, while the large particles and agglomerates remain in the powder bed. Thus, the aerosol characteristics change over time, which also affects the deposition rate and film quality. In contrast, a more consistent dispersion of particles and aerosol quality was obtained in the commercial unit (Figure 9b), leading to a more controllable deposition rate. The disadvantage of that unit was that coarser particles were also aerosolized and introduced into the process, which negatively affected the deposition result.[68] However, by modifying the system with a particle filter downstream of the aerosol unit,[29] this problem could be overcome. Mihara et al. used a modified aerosol unit (Figure 9c), in which mechanical agitation was avoided, and the gas stream (O_2) was split into an aerosol-generating stream and a carrier stream.[58] The aerosol was formed by conducting the aerosol-generating stream into the raw powder at the bottom of the device, and by simultaneously transporting the aerosolized particles into the deposition chamber using the carrier stream. The nozzle, tube, and aerosol generator were heated to reduce moisture. This prevented agglomeration of the barium titanate raw powder used in the study, and enhanced film deposition.[58]

The effect of the carrier gas properties on the PAD process is also a scarcely studied topic. However, the different gas types and their consumption rate affect the pressure in the aerosol chamber and the acceleration of the particles, and in consequence change the kinetic energy of the deposited particles.[2] For example, the density of the carrier gas ρ_g and its velocity ν_g have a considerable influence on the particle drag force F_D, as evident from Equation (2)[19]:

$$F_D = \frac{1}{2} C_D A_P \rho_g (\nu_g - \nu_p)^2 \qquad (2)$$

where A_P is the particles' cross-sectional area, ν_P the particle velocity, and C_D the dimensionless drag coefficient.[19] When using PZT and alumina powders, the impact velocity of the particles increased with increasing carrier gas flow rate,[33] and the

velocity was much higher when He was used as a carrier gas instead of air.[33] Furthermore, the carrier gas type also influences the defect structure of the deposited layers. Akedo et al. studied the transmission properties of deposited PZT films and additionally measured optical emission spectra near the PZT film region during deposition.[56] The 3 and 10 μm thick films deposited using He as a carrier gas were black and had no significant transmittance in the visible-light region of their UV–vis spectra, while films deposited with N_2, O_2, and air were partially transparent and had a brownish color. These results were linked to structural defects, e.g., oxygen defects and scattering defects that may have formed during deposition with He. As optical emissions observed during deposition with He as a carrier gas were absent when using the other gases, it was assumed that these defects are related to electric discharge events in He that accompany the particle impact.[56] Baba et al. also provided evidence for the influence of the carrier gas type on the defect structure of the film.[69] When depositing PZT using O_2, N_2, or He as carrier gases followed by heat treatment, it was found that the electric properties of the films deposited with O_2 and N_2 were superior to those deposited with He. It was suggested that the oxygen and nitrogen radicals remaining at grain boundaries in the films after deposition could compensate for O_2 vacancies forming during heat treatment.[69] In addition, the right choice of carrier gas type also reduced residual stresses inside the material, which are a major problem with aerosol-deposited films.[10] Schubert et al. deposited α-alumina using O_2, N_2, He, and mixtures of the these gases with increasing O_2 content.[11] When using 100% O_2 instead of N_2 and He, the amount of residual stress was halved, and was fully removed after an additional heat treatment below 300 °C. This was explained by the oxidizing atmosphere present during particle deposition, in which a more stoichiometric composition of Al_2O_3 was maintained. Deposition in the absence of oxygen creates oxygen vacancies, which increasingly disturbs the stoichiometry of the material. This was also confirmed by the black color observed for films deposited with N_2 and He, compared to the transparent films deposited in the presence of O_2.[11]

2.3.3. Influence of Carrier Gas Flow Rate and Nozzle Type

Once a suitable powder and a specific carrier gas species have been chosen for PAD, the carrier gas flow rate, usually given in liter per minute, is a determining parameter for the deposition characteristics.[71] Through the flow rate, the particle impact velocity can be controlled.[2,33,77] As described earlier, there is a particle velocity-dependent deposition window with a maximum deposition rate.[2] Cao et al. showed that during the deposition of TiN on glass with otherwise constant parameters, an increase in the flow rate increased the film thickness as well as the hardness and adhesion up to a system-specific maximum value.[71] With a further increase, the film thickness and hardness decreased due to increasing surface damage.[71] This was confirmed by Lee et al. for the deposition of α-alumina particles on different substrates,[44] by Kwon et al. using Fe-based amorphous alloy on soda-lime glass,[36] by Mishra et al. for YSZ particles on different substrates,[37] and by Glosse et al. using magnesium diboride on glass substrates.[19] The latter group also used shadowgraph imaging to study the influence of the gas flow rate and deposition chamber pressure on the gas jet formation between the nozzle and the substrate.[19] With increasing chamber pressure from <5 to 20 mbar, the film thickness decreased, while at constant pressure and increasing flow rate, higher erosion 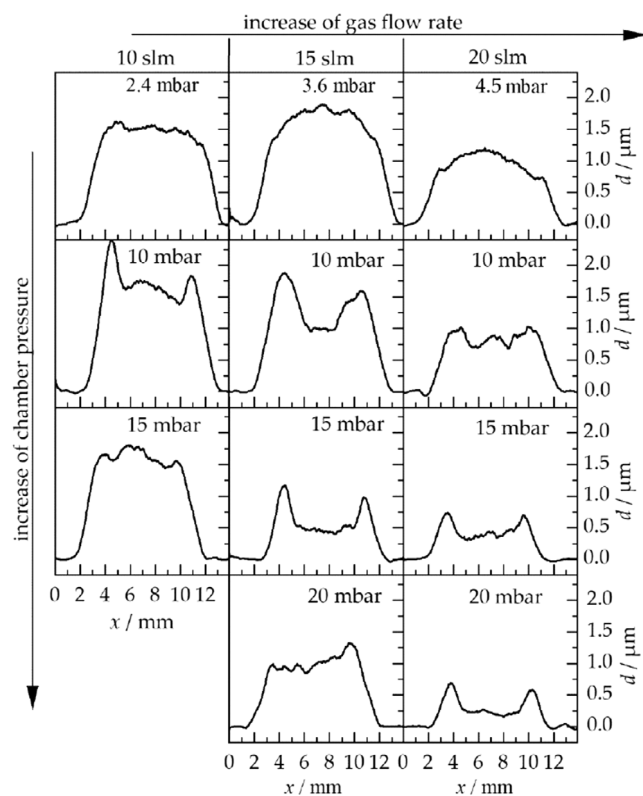occurred (**Figure 10**). At high chamber pressures, pileups occurred at the edges of the films. The authors correlated these pileups with the lateral compression of the gas, leading to an inhomogeneous particle impact across the entire substrate.[19]

The nozzle type influences both the velocity of the aerosol jet and the gas flow field developing between the nozzle and the substrate.[19,44] Two types of nozzles are commonly used in PAD systems: conventional converging nozzles (**Figure 11**a) and converging–diverging nozzles (de-Laval nozzles, Figure 11b).[2] Lee et al. compared three different converging nozzles with varying orifice sizes.[44] They found that the film thickness and deposition rate increased when the nozzle orifice size was reduced, with an optimum size of 1.6×1.6 mm^2 at otherwise fixed deposition parameters.[44] Naoe et al. compared a converging slit nozzle with an orifice of 10×0.4 mm^2 to a de-Laval nozzle with a round throat with a diameter of 3.7 mm and a round exit with a diameter of 8.1 mm.[35] They found that for a wide range of different gas flow rates, the converging slit nozzle caused a higher percentage of surface damage by cavitation than the de-Laval nozzle, indicating a higher particle impact velocity for the converging slit nozzle. In contrast, it was also found that there was no significant difference in DE between converging slit and de-Laval nozzles.[35] Exner et al. obtained improved mechanical and optical properties for alumina films deposited with a de-Laval nozzle compared to a converging slit nozzle and assumed a higher particle velocity in the case of the de-Laval nozzle.[78] Linz et al., in contrast, only found a different film morphology for both nozzle types: a constant film thickness in case of the converging slit nozzle, and a bell-shaped film for the de-Laval nozzle.[21] The aforementioned nozzles have a different influence on the gas flow field between the nozzle and the substrate, which is the reason for the differences in deposition behavior observed.

As the basic principle of PAD is that a fluid (the carrier gas) is transferred from an environment with a certain pressure (the aerosol chamber) to an environment with a significantly different pressure value (the deposition chamber), the question is how this affects the pressure situation in the nozzle. If the pressure at the end of the nozzle is above or below the pressure in the deposition chamber, the nozzle is referred to as underexpanded or overexpanded.[79] In both cases, an undesirable shear layer called Mach disk and/or shock waves form in the gas flow field, which disrupt the deposition process. If the pressure at the end of the nozzle is

Figure 10. Change of the film thickness profile of a magnesium diboride coating with increasing carrier gas flow rate and chamber pressure. Low chamber pressures are required for more homogeneous layers, while a lower flow rate (in standard liters per minute, slm) leads to lower erosion at a fixed chamber pressure. Reproduced with permission.[19] Copyright 2021, MDPI.
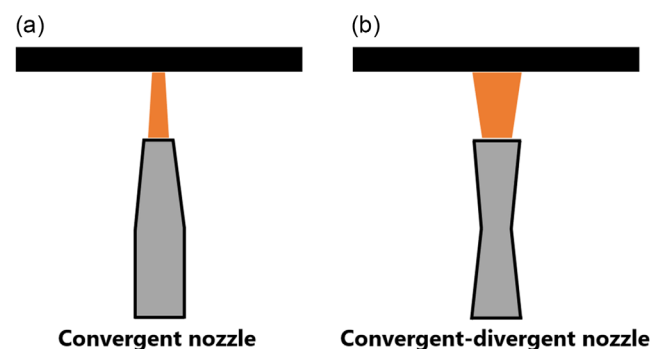

Figure 11. Schematic of the two commonly used nozzles in PAD processes. a) Converging nozzle; b) converging–diverging nozzle (de Laval nozzle).

equal to the chamber pressure, the nozzle is correctly expanded and shock free.[79] Lee et al. studied the de-Laval nozzle in detail using computational fluid dynamics (CFD) simulations in combination with experimental methods.[79] By simulating the flow fields of underexpanded, correctly expanded, and overexpanded nozzles, they showed that in the incorrect cases Mach disks reduce the flow velocity, while shock waves are almost suppressed in the correctly expanded nozzle. This maximizes the kinetic energy of the flowing stream. They validated their results by constructing a correctly expanded and an underexpanded nozzle, and compared the influence on the deposition of TiO_2. While a dense, pore-free film was obtained with the first nozzle, the second nozzle yielded a defective film.[79] The occurrence of shockwaves in a gas flow field simulated by CFD was also shown by Mishra et al. for a converging slit nozzle.[37] Bierschenk et al. studied the effects of nozzle geometry in more detail using CFD simulations, taking into account convergent and divergent nozzles as well as different particle sizes.[80] They found that the gas velocity in converging nozzles is higher than in diverging nozzles, but the particle velocity is higher in nozzles with a diverging section because this extends the flight distance of the particles in areas with higher pressure and higher gas velocity.[80] Furthermore, it was shown that the nozzle throat diameter of converging nozzles only had an influence on the velocity of particles <500 nm, while the length of the diverging region plays a role for all particle sizes investigated. For particles <500 nm, the highest velocities were observed for a converging nozzle with a small nozzle throat diameter, while for particles >500 nm, the highest velocities occurred using a nozzle with a diverging region.[80] All these works indicate that the choice and dimensioning of the nozzle have a significant influence on the deposition result. Fluctuations in the gas flow field of the nozzle can lead to deposition defects even if the parameters are otherwise optimally set.

2.3.4. Influence of Substrate Properties

Particles accelerated through the nozzle of a PAD device are deposited on a substrate via the RTIC mechanism if the conditions for successful deposition discussed earlier are met. The RTIC mechanism in its commonly accepted form is a two-step process in which film formation is only possible once an anchor layer has formed at the interface to the substrate.[2] Therefore, surface properties such as substrate hardness and substrate roughness play an essential role for the deposition process.[11] In one of the first studies on the influence of the substrate, Lebedev et al. investigated the influence of the substrate temperature of stainless steel and quartz glass on the hardness of α-alumina films.[73] They observed an increase in the crystal size and consequently a gradual decrease in film hardness with increasing substrate temperature. No deposition occurred when the temperature exceeded 500 °C. This was explained with an increased plastic deformation of the ceramic particles at higher temperatures, which prevents crack formation and propagation and thus significantly changes the deposition mechanism.[73] In a very recent study, Goto et al. investigated the deposition of alumina on thermoplastic polyurethane rubber as a function of substrate temperature.[81] The rubber substrates were cooled down

from 30 to −65 °C with an unspecified cooling stage before the deposition was started, and the films were compared to a typical PAD alumina film deposited on stainless steel at room temperature regarding the crystallite size, optical transparency and fracture strength (measured with a micro scratch test). Although a PAD film could be deposited on the rubber substrate at 30 °C, the crystallite size in the film was approximately the same as that of the starting powder, meaning that no significant particle size reduction took place. The crystallite size of the film on the cooled substrate, in contrast, corresponded to that of the conventional PAD film on the stainless-steel substrate. In addition, both optical transparency and fracture resistance increased with decreasing substrate temperature.[81] Both works show that the change in the mechanical properties of the substrates with changing temperature has a significant influence on the deposition.

Roughness is another important substrate property. Kim et al. investigated the effect of interlayer roughness on the deposition behavior of alumina.[74] First, they deposited alumina interlayers on an aluminum substrate using the plasma electrolytic oxide method. For this, the aluminum substrate was mounted as an anode in an electrochemical cell with potassium hydroxide and sodium silicate as electrolyte at a voltage of 430 V. This led to the formation of intermediate layers, which exhibited linearly increasing surface roughness with increasing thickness. This made it possible to produce substrates with a defined surface roughness. During PAD, no film growth was observed on alumina interlayers with a surface roughness of $R_a = 1.5\,\mu m$ and above, while deposition occurred on interlayers with $R_a = 0.8\,\mu m$.[74] The authors postulated a roughness-dependent change in the deposition mechanism that either allows or prevents fragment–particle collisions.[74] In the case of the flat and low roughness substrates, impacting particles break into fragments, and these fragments fill the spaces between any protruding surface features. Subsequent particles hit these fragments, which enables the hammering effect, and causes binding of the fragments to the surface (**Figure 12**a,b). For very rough substrates, the particles also break up when hitting the surface, but their fragments are dispersed into the deeper spaces between the jutting surface features, where they cannot be reached by subsequently impacting particles. Thus, the hammering effect cannot occur, and the unbound fragments are removed from the substrate by the carrier gas flow (Figure 12c).[74]

In a similar but more systematic study, Matsubayashi et al. investigated the effect of substrate roughness of silicon substrates with controlled surface microstructure on the PAD of alumina particles.[20] Silicon substrates with line and grid patterns of different spacings were used. SEM images of the cross sections of the resulting materials were taken after PAD deposition (**Figure 13**). The authors found that for samples with line and grid widths of less than 2 μm, the bond between the film and the substrate was weak. In these cases, the space between the surface features was filled with loosely packed fragments, and a continuous, densely packed film was only observed at the height of the protruding parts of the microstructure (Figure 13b–d). For line and space widths larger than 2 μm, a dense and well-anchored film formed over the entire substrate, but the surface contained elevated areas and deep-lying plateaus. Furthermore, a high degree of deformation of the original microstructure was observed (Figure 13e,f). The plateaus formed within the spacings of the
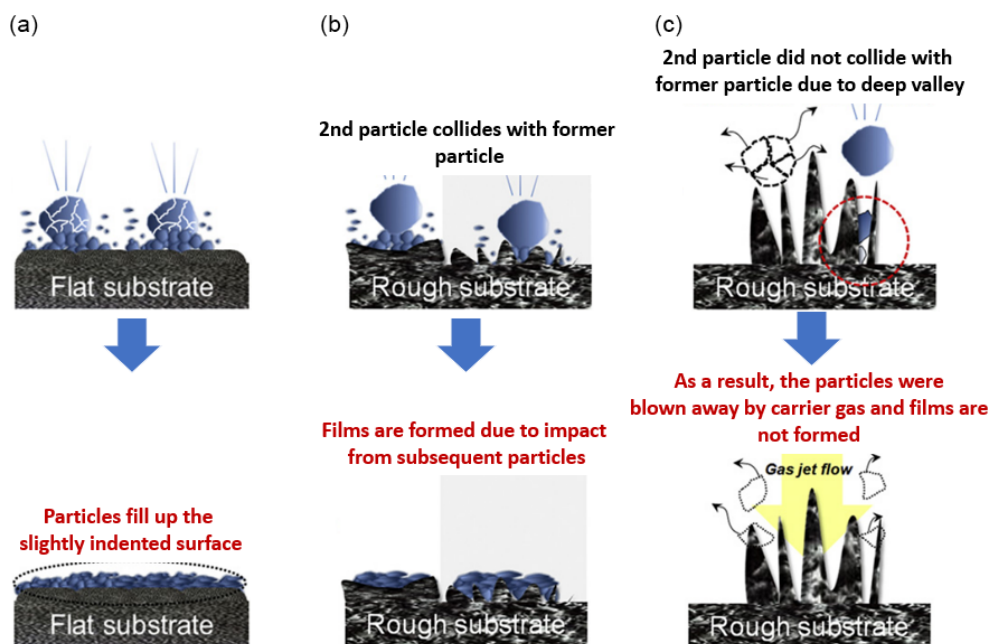
Figure 12. Effect of the surface roughness on the PAD mechanism. Fragmentation and subsequent fragment–particle collisions can take place unhindered on a) flat and b) low roughness substrates, while fragments on c) high roughness substrates are not hit by the following particles and are transported away by the carrier gas flow. Adapted with permission.[74] Copyright 2012, Elsevier Ltd. and Techna Group S.r.l.

original surface microstructures, while the elevated areas of the film were built on the features that were eroded away during the initial deposition. When the substrate surface was unstructured, a dense, well-adhering PAD film with a smooth interface and surface layer formed (Figure 13a).[20] Schubert et al. showed a connection between the substrate roughness and the deposition rate.[31] When depositing alumina on four different substrates with roughness values ranging from $R_a = 0.01$ to $0.95 \, \mu m$, they found a maximum deposition rate in the range of 0.01–$0.2 \, \mu m$, and a decrease at higher roughness values.[31] This is in line with the earlier-observed mechanistic studies which showed that very prominent surface features impede fragment hammering. The earlier-presented data indicates that the effect of surface roughness or distinct surface features in a certain size range is to impede the hammering process. Thus, it is plausible that there are system-dependent threshold values for the width and height of these surface features, and for the ratio of these two values, above and below which the PAD efficiency is strongly reduced. Incoming particles of the typical size range for PAD (0.08–$2 \, \mu m$) will lose a significant amount of their kinetic energy when hitting these surface features before hitting the fragments buried in the spacings underneath. In this context, the size and aspect ratio of the incoming particles and its relation to the roughness or microstructures size, which has not been discussed in the earlier-described studies, should also play a role. Thus, it is important to know both the substrate roughness and particle size before a PAD experiment or when using rough or structured surfaces to find the threshold value for the given substrate–particle combination.

The most intensely studied substrate property in the context of PAD is surface hardness. Akedo et al. suggested that bonding via an anchoring layer requires a substrate with suitable hardness and elasticity.[29] Substrates that are too soft are etched by the particle jet, and substrates that are too hard do not provide sufficient adhesive strength.[29] This was confirmed by a number of experimental studies which ascertain that the formation of anchoring layers is facilitated by softer substrates,[17,44,46,48–50] and that these have better film adhesion than harder ones.[48] No or not visible anchoring layers were formed on hard substrates, yet in some cases, a PAD film was still obtained in such systems.[31,44] Khansur et al. examined the effect of surface roughness, microstructure, residual stresses, and surface free energy of stainless-steel substrates on the resulting films.[49] They deposited NaCl films on different substrates and removed them by washing to expose the PAD-treated surface. In line with the previously discussed reports, they found that the ductility of a substrate is important for the formation of an anchoring layer. Furthermore, they postulated a change in the surface free energy of the stainless-steel substrate after PAD: the water contact angle on PAD-treated surfaces showed a slight decrease, while the contact angle of nonpolar diiodomethane on these surfaces significantly increased in comparison to the situation before the PAD process. Using the Owens, Wendt, Rabel, and Kaelble method, this was related to a change in surface energy from $37 \, mN \, m^{-1}$ before the PAD process to $31 \, mN \, m^{-1}$ after the PAD process. They correlated these findings with increased dipole moments on the substrate, indicating that adhesion in PAD is a combination of mechanical and chemical interactions.[49] Care must be taken when interpreting this data. PAD is an abrasive process even in cases where a film eventually forms. Thus, it will change the surface properties of the PAD substrate in a number of ways, including removal of any surface-attached hydrocarbon impurities or native oxide layers, and increase of the surface roughness. Thus, it is difficult to assign changes in surface energy after PAD to distinct molecular processes on the surface. Khansur et al.
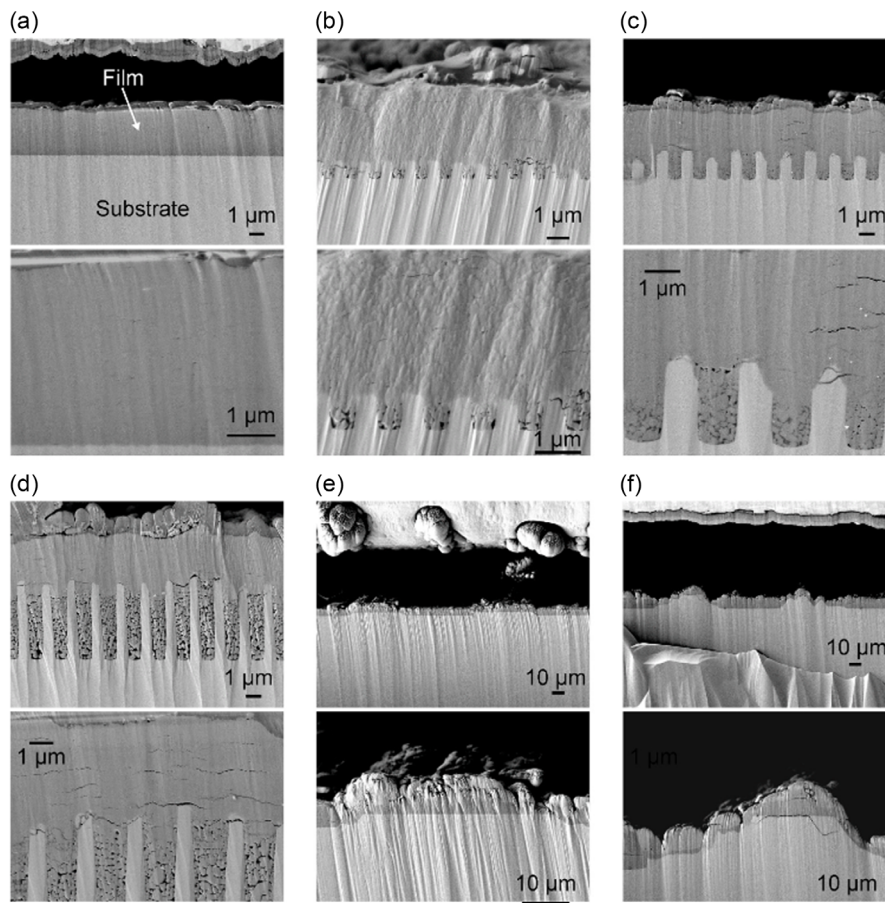
Figure 13. SEM cross sections of alumina deposited on silicon surfaces with different microstructures. a) Polished substrate; b) line and space width (w) = 0.5 μm, line height (h) = 1 μm; c) w = 1 μm, h = 2 μm; d) w = 1 μm, h = 10 μm; e) w = 50 μm, h = 2 μm; and f) w = 50 μm, h = 10 μm. Reproduced with permission.[20] Copyright 2023, Elsevier Ltd. and Techna Group S.r.l.

additionally reported high residual compressive stresses on the surface of the substrates after PAD (−587 MPa) compared to the pre-PAD state (−26 MPa). They speculated that the ability of the substrate to absorb the residual stresses generated by the deposition could be a prerequisite for anchor layer formation.[49]

Since film adhesion on certain hard substrates was also observed, it is assumed that other modes of adhesion in addition to anchor layer formation exist, which may include ionic or covalent bonds. These have already been measured for alumina deposited on soft Cu substrates,[45] which confirms their general existence, but were not yet explicitly proven for hard substrates. It was assumed that there is a higher impact pressure on hard substrates,[48] and that fracturing of particles and densification of the layer is also enhanced on these materials.[17,43,46,48,50,82] Kim et al. investigated the anchoring effect and densification on substrates with different hardness and melting points (stainless steel, Al, Sn, BMG) when depositing Y_2O_3.[46] They found an increased anchor layer thickness and lower densification in SEM and TEM cross sections of the Sn substrate, which has a low melting point, while they reported low anchoring and high densification on Al and stainless-steel substrates, which have higher melting points. High anchoring and high densification were also achieved when Y_2O_3 was deposited on BMGs.[46]

The authors speculated that the particle impact led to a local temperature increase above the glass-transition temperature of the BMG, allowing plastic deformation of the supercooled liquid along with an enhanced buildup of the anchoring layer. Densification was promoted by the high hardness of the BMG compared to the other substrates.[46]

In summary, the main parameters that influence the PAD process are the powder characteristics and pretreatment, the mode of aerosol generation and carrier gas type, the carrier gas flow rate and nozzle type, as well as substrate properties. It turns out that successful deposition depends on the complex interplay of these parameters. Researchers have only just begun to understand this interdependency, and future work should focus on this aspect, in particular when working with new substrate–particle combinations.

2.4. In Silico Work Investigating the Deposition Mechanism and Parameters

During the PAD process, microscopic particles hit a substrate at very high speed and are subsequently deformed at a high strain rate. For such processes, direct experimental evidence leading to

**ADVANCED
SCIENCE NEWS**

www.advancedsciencenews.com

**ADVANCED
ENGINEERING
MATERIALS**

www.aem-journal.com

the elucidation of the underlying deposition mechanism is only possible to a very limited extent. Therefore, in silico work dealing with the physical and atomistic processes during the impact of the particles is an important tool to clarify the deposition mechanism. The variables of interest are mainly the particle and impact velocity; the evolution of pressure, temperature and strain fields in the particle and substrate during impact; and the associated macroscopic deformation and microstructural processes within the particle and substrate that contribute to binding.

The relevant literature in this context can be classified by the underlying simulation method into CFD simulations, mostly in combination with finite-element methods (FEM)[33,38,39,51,77,83–93] and molecular dynamics (MD) simulations.[13,94–102] CFD simulations are mainly used to investigate the dynamic behavior of the particles and the carrier gas, and in combination with FEM, the evolution of the field-distributed quantities in impacting particles and the substrate. MD simulations rather aim to understand the deformation and bonding to the substrate via atomistic processes. Although these studies mainly concern inorganic materials, which is not the focus of this review, they will be included in detail due to their importance for understanding the PAD mechanism.

The change in particle or impact velocity on the deposition mechanism has been studied in great detail.[51,77,83–85,91–94,98,100–102] A CFD simulation was performed by Park et al. for a one-particle impact of 0.3 µm Al_2O_3 particles on Al_2O_3 and glass substrates using the Johnson–Holmquist 2 (JH-2) material model.[85] At low impact velocities, the particles elastically rebound at the substrate without major deformation (**Figure 14**a,d), while at a velocity of $50\,m\,s^{-1}$ for the Al_2O_3 substrate and $100\,m\,s^{-1}$ for the glass substrate, a tensile stress was generated vertically to the impact direction, which induced fragmentation in addition to the elastic rebounding (Figure 14b,e).[85] With a further increase in the impact velocity, the material behavior changed from elastic

rebounding with fragmentation to bonding to the surface with both fragmentation and plastic deformation of the particle (Figure 14c,f). While the velocity at the first transition was referred to as the threshold velocity, the second velocity was referred to as the critical velocity. It was determined to be $150\,m\,s^{-1}$ for the Al_2O_3 substrate, which corresponds to the experimentally determined value of Akedo et al.,[33] and $350\,m\,s^{-1}$ for the glass substrate.[85] This confirms the assumption that the critical velocity for successful deposition is material dependent, as also shown in a CFD simulation of SiC particles impacting on Zr alloy and SiC at different particle velocities.[91] Both studies also showed that the impact pressure increased with increasing particle velocity and is higher for softer substrates than for hard substrates.[85,91] In a later work, Park et al. extended their simulation to include polycarbonate (PC) substrates.[51] In addition to a previously described threshold velocity of $300\,m\,s^{-1}$ for Al_2O_3 particles impacting on PC, no critical velocity associated with fragmentation and plastic deformation of the particles was found within the simulated velocities. Instead, only an indentation of the undeformed particles with adhesion to the substrate surface was observed. By analyzing the energy balances of the simulated impact experiments, an increase in both the internal energy of the substrates and the impacting particles could be noted for the glass and Al_2O_3 substrate, while in the case of PC, only the substrate internal energy increased. From this, the authors deduced that with very soft substrates, the entire kinetic energy of the particles is consumed by the deformation of the substrate, by which process the impacting particles are also bound. For this system, fragmentation and plastic deformation of the particles was not very pronounced, which the authors related to the shock-absorption effect.[51]

While the previous section mainly described PAD processes with changing particle velocity, the following section will focus
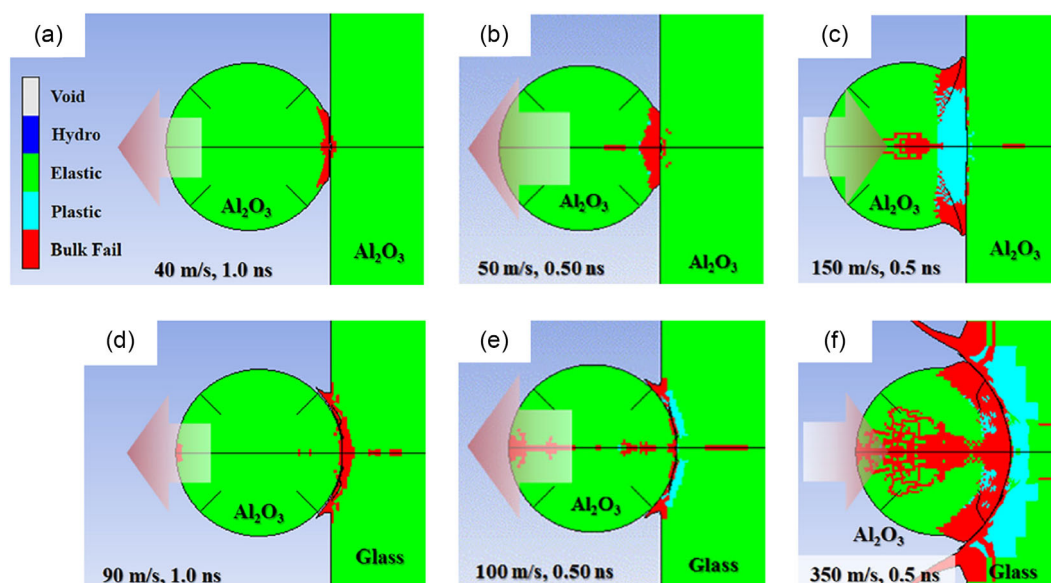

Figure 14. CFD simulation of the one-particle impact of Al_2O_3 particles on Al_2O_3 and glass substrates with increasing impact velocity. Impact of an Al_2O_3 particle on Al_2O_3 substrates a) below the threshold velocity, b) above the threshold velocity, and c) above the critical velocity. Impact of an Al_2O_3 particle on glass substrates d) below the threshold velocity, e) above the threshold velocity, and f) above the critical velocity (direction of the red arrow indicates rebounding or bonding). Adapted with permission.[85] Copyright 2016, ASM International.

on simulations that were carried out above the critical velocity. Akedo et al. simulated the impact of 0.3 μm Al_2O_3 particles hitting a silica glass substrate at the previously experimentally determined critical velocity of 150 m s^{-1} using FEM and the JH-2 material model.[33] They observed an increase in pressure above the fracture strength of the material and a temperature increase far below the melting temperature of the particles, from which they concluded that the PAD process is more mechanically than diffusion controlled.[33] This result was confirmed in further work using various simulation methods and different systems.[38,77,85,91–93,95,98,100–102] Chun et al. used a CFD simulation with the JH-2 material model to study the single- and two-particle impact of 0.5 μm Al_2O_3 particles impacting on Al_2O_3 substrates with a velocity of 350 m s^{-1}.[38] While the first particle impact led to a maximum pressure of 5.7 GPa and a maximum temperature of 600 K close to the particle–substrate interface, the impact of the second particle produced an increase in temperature and pressure at the interface between the first particle and the substrate that was larger than in the one-particle case.[38]

Within the theory of the deposition mechanism, this can be seen as evidence for the hammering effect. In two other studies, Kwon et al. investigated the development of pressure and von Mises stress fields using CFD simulations of Y_2O_3, Al_2O_3, and SiO_2 on substrates made from the same material, respectively.[77,92] As shown in **Figure 15**a for a 1 μm Y_2O_3 particle impacting on a Y_2O_3 substrate at 300 m s^{-1}, the pressure in both the particle and the substrate increased in a very localized area around the contact point.[92] While the pressure field did not spread significantly further with increasing simulation time—the authors speak of a confining pressure—the propagation of a shock wave from the contact point into both the substrate and the particle could be observed in the development of the von Mises stress. As a result, the von Mises stress in parts of the particle exceeded the elastic limit and the particle deformed plastically. With increasing simulation time (Figure 15b), material failure occurred first in the edge elements of the particle due to the absence of confining pressure, while finally complete fracture of the particle occurred due to the complete reduction of confining pressure.[92]
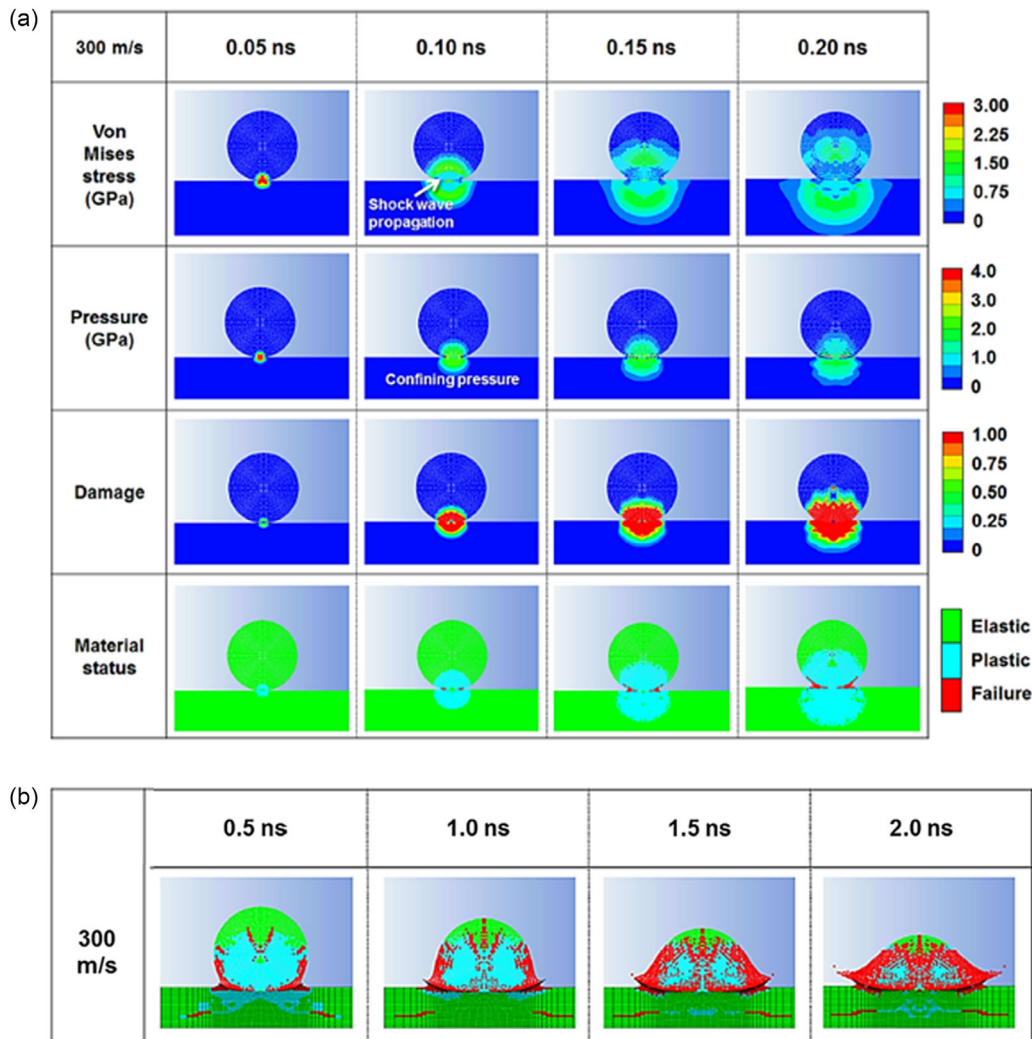

Figure 15. CFD simulation of the one-particle impact of Y_2O_3 particles on Y_2O_3 substrate at 300 m s^{-1}. a) Development of different simulated parameters in the early stage of simulation. b) Material status at longer simulation times. Adapted with permission.[92] Copyright 2020, Elsevier B.V.

This behavior was referred to as dynamic fragmentation[77,84,92] and is contrasting the RTIC mechanism proposed by Akedo, in which fragmentation and plastic deformation are regarded more or less as two independent processes.

A very crucial point in simulative work investigating the deposition mechanism is the change in microstructure within both the particle and the substrate during particle impact. MD simulations are much better suited for this because, unlike CFD simulations, they are not based on a continuum, but on the interaction of individual atoms, which enables the mapping of microstructural changes on the basis of atomistic processes. In three series of MD simulations carried out by Ogawa,[94–96] Daneshian,[13,97,99] and Song et al.,[100–102] the atomistic processes during the deposition were studied. Ogawa investigated the impact of 10 nm ZrO_2 particles on ZrO_2 substrates at velocities of 250–2000 m s^{-1} in a first MD simulation using the interatomic potential of Darivedi and McCormack.[94] It was found that impacting particles break via slipping starting at a velocity of 500 m s^{-1}, while at velocities above 1500 m s^{-1}, disordered phases are formed in addition to crystalline fragments.[94] Since slip processes essentially depend on the underlying crystal system, Ogawa investigated the impact of 10 nm body-centered cubic iron and face-centered cubic (fcc) nickel at 1000 m s^{-1} in a further study.[96] In addition to orientation changes within the impinging particle, it was also observed that the crystal orientation of the particle expanded into the substrate, similar to crystal growth. Furthermore, Ogawa reported the formation of a third phase at the interface between substrate and particle, which formed due to surface energy minimization.[96] This could indicate the formation of an anchor layer. All the microstructural changes mentioned earlier were also observed for fcc Ni, but to a lesser extent, which was attributed to the lower number of active slip systems in the fcc lattice. In a more detailed work, Daneshian et al. used MD simulations to investigate the deformation processes during single-particle impacts of single-crystalline brittle nanoparticles of not a specified material as a function of particle size.[13,97,99] To generate brittle material

behavior, they used a Lennard–Jones potential with a defined cut-off radius, which was previously adjusted based on results from simulated tensile tests.[13,97,99] They found that above a certain particle size, the deformation behavior of the particles changed from fragmentation without attachment to the substrate to plastic deformation with attachment to the substrate.[97] This particle-size-dependent brittle-to-ductile transition was considered to be central to the PAD mechanism and was later confirmed by Kuronayagi et al. using microcompression experiments on Al_2O_3 particles.[103] In a subsequent study, Daneshian et al. also investigated the deformation of the particles in a low-strain-rate compression test and on impact in detail.[13] When comparing the development of the stress, shear, and temperature fields during the simulation of the two experiments (**Figure 16**), a similar deformation behavior was found, which was characterized by local inelastic deformation along slip systems (at about 45° to the load) and shear band formation in the shear strain signal. However, while in the case of the low strain rate simulation, the shear bands ran through the entire particle (Figure 16a), in the case of high strain rate impact, they developed locally at the point of impact of the particle in the form of a shear cone, which spread into the particle as the simulation time increased (Figure 16b). Crack formation was suppressed within this shear cone, and the temperature increased significantly.[13] In a series of very recent MD simulations of the PAD process, Song et al. simulated various aspects of the deposition process.[100–102] To gain a deeper insight into the changes in the crystal structure during particle impact, they simulated the deposition of 60 nm fcc Ni particles on Ni substrates at particle velocities of 750–1500 m s^{-1} using large-scale atomic/molecular massively parallel simulator software with the embedded-atom potential.[101] A loss of crystallinity was observed during the impact, but with increasing simulation time, recrystallization was observed mainly at the particle–substrate interface. This was driven by the incorporation of Shockley partial dislocations into the fcc grains, as can be seen in **Figure 17** for the microstructure at 20% total strain for the 60 nm Ni particles (Figure 17a,b), and at the end of the
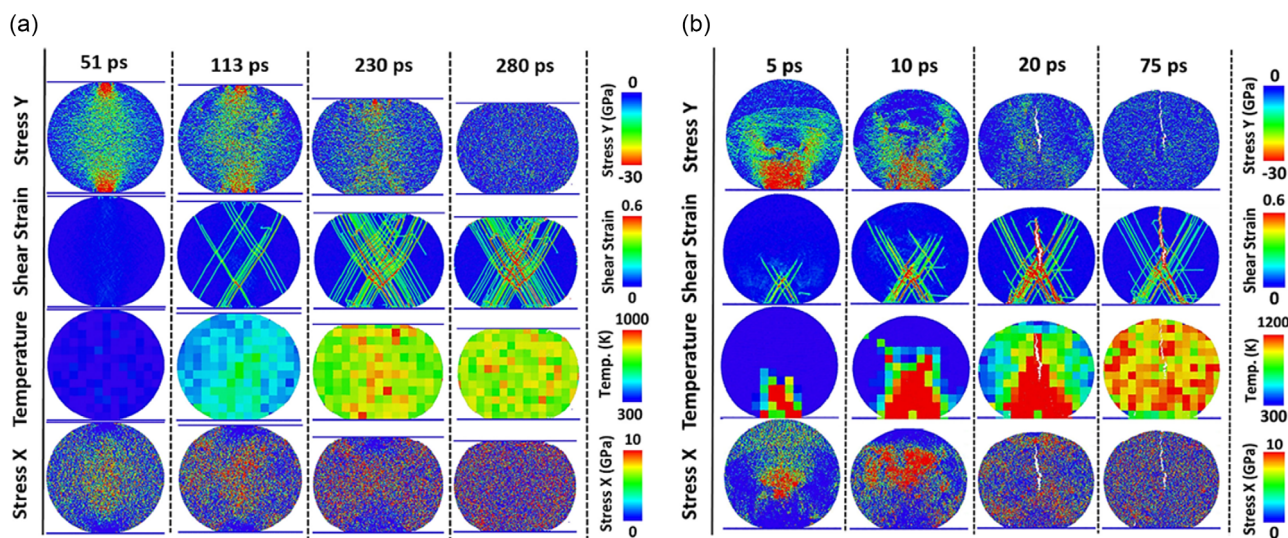

Figure 16. MD simulation of the deformation behavior of a 50 nm TiO_2 particle. Development of different simulated parameters in a) low-strain-rate microcompression test and b) high-strain-rate impact on a rigid substrate. Adapted with permission.[13] Copyright 2021, Springer Nature.
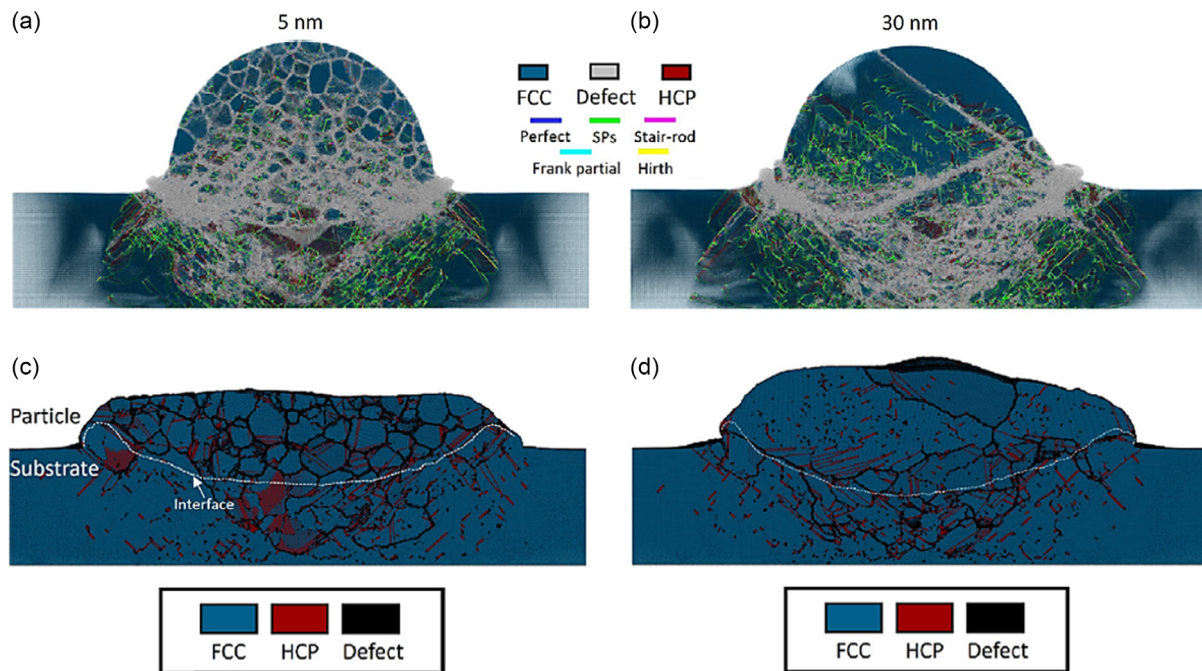
Figure 17. Microstructure of Ni particles impacting on Ni substrates at 1500 m s⁻¹. Microstructure of a 5 nm Ni particle at a) 20% total strain and c) the end of the simulation. Microstructure of a 30 nm Ni particle at b) 20% total strain and d) the end of the simulation. Adapted with permission.[101] Copyright 2023, Elsevier Ltd.

simulation for 5 and 30 nm Ni particles impacted at 1500 m s⁻¹ (Figure 17c,d).[101] As Daneshian et al. found before, deformation was driven by the formation of shear bands. It should also be noted that with small grain sizes, deformation mainly occurred via grain boundary movement, whereas with larger grain sizes it was more likely to be caused by dislocation movement.[101] In a subsequent MD simulation, the same group investigated the single-particle impact of 100 nm Bi particles at 500 and 600 m s⁻¹ on Bi substrates, and the impact of two Bi particles next to each other.[102] For the single-particle impact of the Bi nanoparticle, a maximum temperature of 980 K for 500 m s⁻¹ and 1300 K for 600 m s⁻¹ was obtained.[102] By specifying a melting temperature of 558 K for Bi, the authors proved that the temperature rise during the PAD process can very well be above the melting temperature for low-melting materials. As a result, the deposited particles showed a splat-like, amorphous structure with some ejected parts. For the multiparticle case, no higher maximum temperature was obtained for the impact of the two Bi particles compared to the single-particle case, but it could be seen that the temperature fields in the respective particles interacted with each other, resulting in coalescence of the two particles.[102]

The work presented in the following mainly focused on investigations of the gas flow field,[37,80,88–90,93] and the resulting effects on deposition. This was done exclusively via CFD simulations. Park et al. simulated the gas flow field of He and N₂ as a function of the pressure difference between the aerosol chamber and the deposition chamber and found that the velocity of both gases was reduced with increasing outlet pressure.[90] At the same time, they found that the effect was less pronounced with increasing material density of the deposited particles. The difference between the average and impact velocity was greatest for

polyimide (PI), which had the lowest density.[90] Li et al. investigated the influence of the pressure difference in more detail by simulating 3–10 μm silica and copper particles with N₂ as a carrier gas. In addition to simulating the gas flow field by solving the 2D compressible Navier–Stokes equations and using this data to calculate the particle drag force (as usually done in CFD of the PAD process), the simulation was additionally performed by a neural network. Direct simulation Monte Carlo results were used to determine the drag coefficients more precisely. The authors found that the influence of the pressure difference on the particle velocity was superimposed with a particle size effect (**Figure 18a**). Based on the maxima in Figure 18a, they deduced that there is a particle size with maximum impact velocity which, in addition to the pressure in the aerosol bottle, is also dependent on the density and the nozzle geometry. To explain this, Li et al. considered the gas velocities within the gas flow field between the inlet of a converging–diverging nozzle (corresponding to 0 mm on the x axis) and the substrate surface (corresponding to 66 mm on the x axis), as shown in Figure 18b (nozzle outlet at 60 mm on the x axis). While the gas velocities increased to a constant value (from <100 to about 600 m s⁻¹ for the 760 Torr case and to about 500 m s⁻¹ for the 190 Torr case) at the transition from the converging to the diverging part of the nozzle (25 mm on the x axis), they sharply increased at the exit of the nozzle, followed by a drastic drop in velocity to almost 0 m s⁻¹.[88] This is known as a shock in the gas flow field and has already been described earlier in the chapter on the influence of carrier gas flow rate and nozzle type. Li et al. assumed that due to the low inertia of small particles, they are slowed down too much by this shock, while particles that are too large are not significantly affected due to their higher inertia, but cannot be fully accelerated within the nozzle.[88] As a
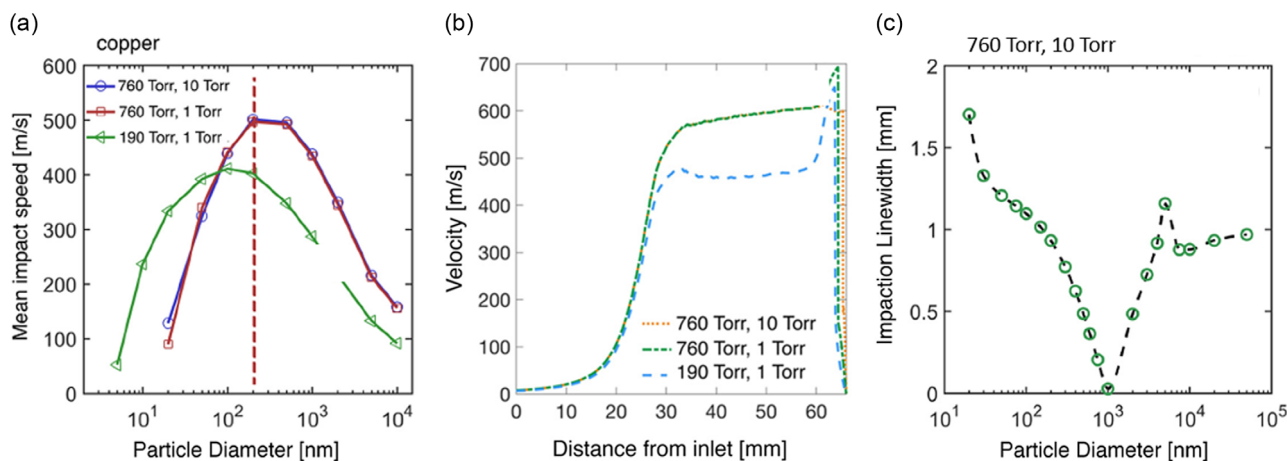
ADVANCED
SCIENCE NEWS
www.advancedsciencenews.com

ADVANCED
ENGINEERING
MATERIALS
www.aem-journal.com

Figure 18. Impaction behavior of copper particles with varying pressure difference. a) Mean impact speed for different pressures in the aerosol and deposition chamber as a function of particle diameter. b) Gas velocity as a function of the nozzle inlet position at the aerosol chamber side. c) Impaction linewidth (defined as four times the average impact position on the substrate according to the symmetry condition of the simulation) for the 760 and 10 Torr cases as a function of particle diameter. Adapted with permission.[88] Copyright 2018, Elsevier Ltd.

result, the impact location of these particles on the substrate changes (Figure 18c). The authors describe particles that are too small as underfocused and particles that are too large as overfocused, analogous to optical systems. Li et al. demonstrated that optimally focused particles have an optimal transfer of the particle kinetic energy to the substrate, and that PAD setups should be designed with these particles in mind in the future.[88] While these findings are very interesting within the context of this review, they can be regarded as technically very difficult to realize, as this would involve not only the implementation of the particular PAD system in this simulation formalism to determine the optimal particle size, but also the production of monomodal powders based on these results, which is not possible in every case.

In summary, simulative work confirmed key aspects of the theory of the PAD process that were previously derived from experimental results, such as the occurrence of a critical velocity and an effective deposition window, or the influence of a brittle-to-ductile transition on successful deposition. Additionally, simulative work has shown that the microstructure of the deposited film can be predicted in detail, and contributes to finding parameters for successful deposition without the need for major parameter studies. Also, it should be possible to increase the efficiency of the process on the basis of simulated results.

3. PAD as Preparation Method for PCCs

The combination of inorganic materials like ceramics or glasses and organic components such as polymers leads to new materials with multiple functionalities and properties. Natural representatives of such combination materials or composites are bone, dentin, or nacre. In these materials, the brittle, inorganic components are combined with a low percentage of organic molecules to achieve an optimum between strength and toughness, which is often mutually exclusive in single-component materials.[104] Since these biological structures are made by self-assembly and have a rather complex microstructure,[105] processes that try to emulate

them in synthetic materials are often time-consuming, expensive, and difficult to implement.

Polymer matrix composites (PMCs) are synthetic materials where a dispersed phase (particles, fibers, or nanomaterials) are incorporated in a continuous phase, the polymer matrix, to increase the mechanical performance or provide further functionalities.[106] PMCs with particles are difficult to fabricate due to particle agglomeration, an effect which increases with increasing filler concentration, and which reduces the positive properties of the material combination due to an inhomogeneous bulk distribution.[107–109] This problem can be solved with elaborate particle processing, so that composites consisting of a polymer matrix and a ceramic filler are accessible. However, composites with a ceramic matrix (CMCs) and a dispersed polymer filler cannot be obtained by traditional ceramic processing techniques because high temperatures are needed to sinter the ceramic after addition of the polymer particles. These temperatures are far above the decomposition temperature of most polymers.

Fortunately, PAD provides an avenue to obtain such materials. As described earlier, the PAD process gives access to composite films made from powder mixtures of two or more components by AcD. AcD yields dense films with uniformly distributed components, which can be used to adjust the electrical and mechanical properties of the film.[2] As it is a room-temperature process, the combination of polymers and ceramics is possible in PAD. The high temperatures that can locally and shortly develop during particle impact are far below ceramic sintering temperatures and are tolerated by many polymers. This chapter reviews studies in which the combination of polymers and ceramics in the PAD process was investigated. These reports can be subdivided into three groups. The first group consists of papers that investigate ceramic layers deposited on polymer substrates.[24,51,81,110–116] In the second group, polymer powders are used in combination with ceramic powders as a sacrificial phase to create porous structures.[117–120] Research that focused on the deposition of a PCC film without removal of the organic component forms the third group.[4,28,62,114,121–131]

**ADVANCED
SCIENCE NEWS**

www.advancedsciencenews.com

**ADVANCED
ENGINEERING
MATERIALS**

www.aem-journal.com

3.1. Polymer Substrates

As has been discussed previously, the substrate hardness is crucial for successful PAD. In this context, polymer substrates, which are much softer and much more ductile than glass, metal, or ceramic substrates, have been investigated. Different types of—mostly inorganic—powders were deposited on polymer substrates, e.g., TiO_2 on polyethylene terephthalate (PET) and poly(methyl methacrylate) (PMMA)[110]; $Bi_{1.5}Zn_{1.0}Nb_{1.5}O_7$ (BZN) and copper on PI[111,112]; hydroxyapatite (Hap) on poly-L-lactic acid[113]; a magnetic composite powder made from polytetrafluoroethylene (PTFE) and Fe–Si–Cr flakes on PET[114]; graphite on polystyrene (PS)[115]; Al_2O_3 on PC[33,51] and thermoplastic polyurethane rubber[81]; as well as Bi_2Te_3 and lunar mare simulant on Kapton and Mylar foils.[24,116]

In a very detailed study using experimental and numerical methods, Park et al. investigated the deposition of alumina on a PC substrate in comparison to glass and alumina substrates.[51] With the PC substrates, they observed less fragmentation and more rebound of the particles, resulting in an unusual interfacial microstructure with two distinct regions, one near the substrate (Region A, **Figure 19**a) and the other above (Region B, Figure 19a). Region A consisted of initially impacted particles which were only slightly fractured (Figure 19b). Additionally, no lattice distortions of the alumina were found in high-magnification TEM images of

these particles (Figure 19c). The authors interpreted the near-substrate film as an anchoring layer. In Region B, in contrast, severely fractured particles (Figure 19a) with randomly oriented nanocrystals (observed in HR-TEM, Figure 19d) were found. Apparently, the initially impacting particles first penetrate the outer surface of the comparatively soft substrate and remain intact, while the subsequent particles follow the RTIC mechanism as described for metal and ceramic substrates. The initial penetration of particles into the polymer substrate was described as a shock-absorption effect, in which part of the kinetic energy of the particles is converted into internal energy of the substrate rather than leading to fracture and deformation of the particles.[51] The shock-absorption effect has also been observed for PAD on other polymeric substrates[81,114,115]; for example, in the work of Kim et al. who deposited magnetic composite powders of Fe–Si–Cr and PTFE on PET and glass substrates.[114] While no film formation was possible on the glass substrate, a well-adhering, dense PAD film formed on the PET substrate. With increasing concentration of PTFE powder, the deposited film became more porous and less adhesive, which was attributed to a reduced fracture of the Fe–Si–Cr flakes due to the more pronounced shock-absorption effect of the PTFE particles.[114] Al-Nasim et al. obtained PAD films of graphite on PS, copper, glass, and sapphire.[115] They observed less fragmentation and a less dense film with large voids on the PS substrate, and a higher film thickness compared to the other
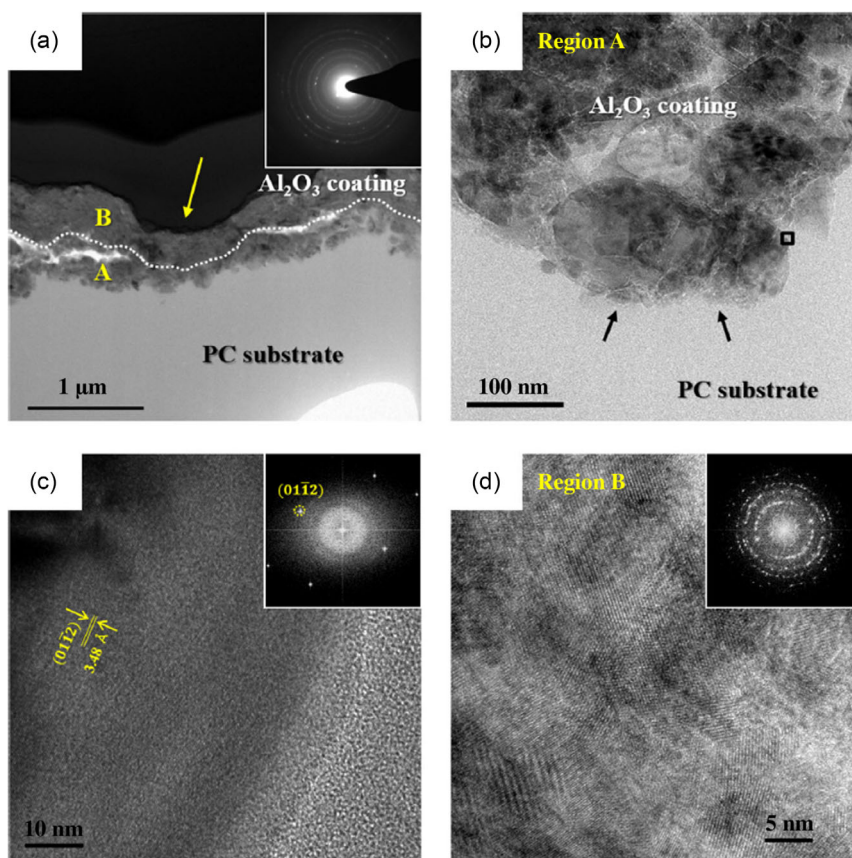
Figure 19. TEM cross sections of alumina films deposited on a PC substrate. a) Two distinct regions were observed for an alumina coating on a PC substrate: b) Region A consists of almost intact, deeply penetrating particles. c) No lattice distortions were visible in the high-magnification image of the black inset of (b). d) Randomly oriented nanocrystals were found in Region B. Reproduced with permission.[51] Copyright 2020, ASM International.
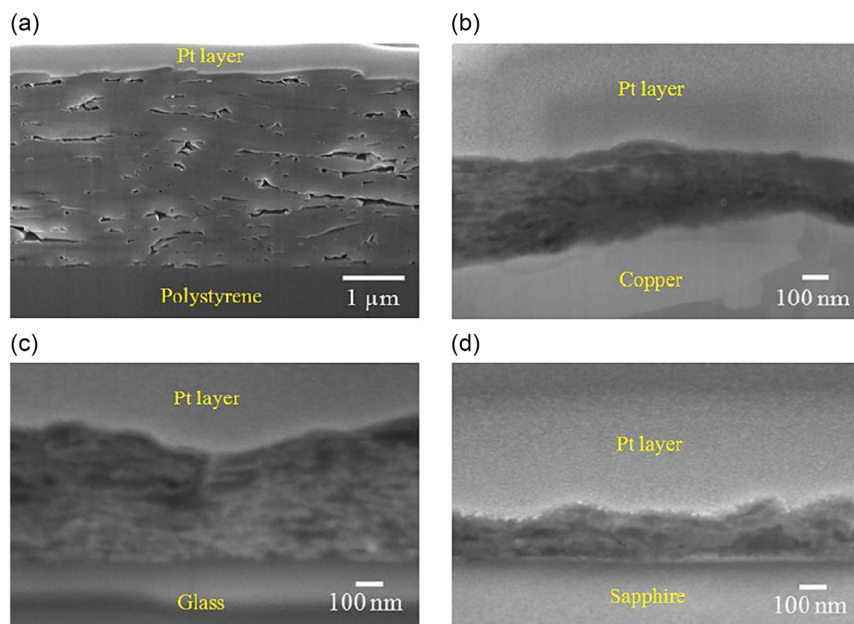
**ADVANCED
SCIENCE NEWS**

www.advancedsciencenews.com

**ADVANCED
ENGINEERING
MATERIALS**

www.aem-journal.com

Figure 20. Cross sections of graphite films deposited on different substrates imaged by SEM. All samples were platinum (Pt) coated after PAD. a) A thick, but less dense graphite film with large pores formed by PAD on a PS substrate. Only thin graphite films could be deposited by PAD on b) copper, c) glass, and d) sapphire substrates. Reproduced with permission.[115] Copyright 2016, Elsevier B.V.

substrates (**Figure 20**a–d). This was also associated with the shock-absorption effect.[115] Goto et al. deposited alumina on thermoplastic polyurethane rubber at different substrate temperatures (from 30 to −65 °C).[81] In a PAD film deposited at 30 °C, the crystallite sizes in the film were approximately the same as in the starting powder due to the pronounced shock-absorption effect of the substrate. In contrast, the crystallite sizes of the film that formed on the cooled substrate were significantly smaller. In addition, the optical transparency and fracture resistance of the films increased with decreasing substrate temperature.[81]

The authors explained this with the change in the mechanical properties of the substrate when lowering the temperature below the glass-transition temperature of the rubber.[81] This work demonstrates that the shock-absorption effect can be influenced both by the choice of substrate and the process temperature. This opens new possibilities for adapting the PAD process for polymer substrates.

The interest in PAD on polymer substrates is due to their mechanical flexibility and low weight. With these properties, applications in the field of flexible electronics can be envisioned. Ryu et al. deposited films of BZN dielectric ceramics on copper-coated PI foils.[111] The coated films had a dense microstructure, a high dielectric constant and good adhesion even during strong bending.[111] Werner et al. coated flexible Kapton and Mylar films with Bi_2Te_3 and investigated the thermoelectric properties and their dependency on the bending radius.[24] They found that the thermoelectric properties of the films decreased with increasing bending radius, but partially recovered when the load was removed.[24] In addition, they observed changes in the microstructure of the films after bending, while the adhesion of the films remained unchanged.[24] A detailed study on the mechanical properties of PAD films on polymer substrates was carried

out by Calvo et al. using lunar regolith deposited on Kapton.[116] The films produced showed excellent adhesion and abrasion properties in the mandrel bending test and scratch test, which was attributed to a pronounced anchor layer between Kapton and the PAD film. In addition, tensile tests of coated samples compared to uncoated Kapton showed a higher elastic modulus and a lower elongation at break. Furthermore, the coated films had a high degree of inherent bending, indicating residual stresses in the PAD layer.[116] In summary, the inherent ductility of polymers causes mechanistic changes during the PAD process, but also gives access to a applications that are not accessible with metallic or ceramic substrates.

3.2. Polymers as Sacrificial Phase

Porous ceramic materials have a wide range of applications including catalyst supports, filter membranes, and substrates for electrochemical electrodes. The main processing routes to obtain such materials are partial sintering, replica templates, direct foaming, or the use of a sacrificial agent.[132] AcD of polymer and ceramic powders via PAD belongs to the latter group of processes. After deposition of the composite material, the polymer component is burnt out. For example, polyethylene glycol (PEG) and polyvinylidene fluoride (PVDF) were used as sacrificial polymer phases.[117–120] In work by Fan et al., nanoscopic TiO_2 powder was dispersed in ethanol and mixed with different amounts of a PEG solution (weight average molar mass 10.000 g mol^{-1}). This resulted in colloidal particles with different PEG content (9.1%, 23.1%, 37.5%, 41.2% by weight). After drying in an evaporator and crushing with a mortar, both the composite powder and pure TiO_2 powder were deposited onto indium-tin-oxide-doped conducting glass substrates by PAD.[117] Both

**ADVANCED
SCIENCE NEWS**

www.advancedsciencenews.com

**ADVANCED
ENGINEERING
MATERIALS**

www.aem-journal.com

materials gave films with a porous microstructure. They were combined with a counter electrode to produce a sandwich-like dye-sensitized solar cell. The PAD films were sintered at 450 °C, which led to a burnout of the PEG and an increase in porosity compared to the pure titanium oxide layer, which enhanced the performance of the dye-sensitized solar cell.[117] Choi et al. co-deposited various mixtures of PVDF with either a piezoelectric ceramic powder (PMNZT)[118] or a (La,Sr)(Co, Fe)$O_{3-\delta}$ perovskite oxide ceramic[119] on different substrates. In both cases, the deposition was successful, regardless of the PVDF content. In addition, X-ray scattering showed larger particle sizes in the composite PAD film compared to the pure ceramic film, which was explained by a reduced particle fracture during deposition due to the shock-absorption effect of the PVDF particles.[118,119] Co-depositing PMNZT with 3, 5, or 10 wt% of PVDF gave layers with homogeneous nanoporous morphology after heat treatment at 700 °C, where the porosity was influenced by the concentration of PVDF in the starting powder (**Figure 21**a–i).[118]

These few studies demonstrate that AcD of polymer and ceramic powders yields thin, porous ceramic films with well-defined morphology. The advantage of the process compared to conventional sintering processes is that the film morphology is already formed before the heat treatment, and that only temperatures sufficient to burn out the polymer component need to be applied, which are much lower than that those for sintering.

3.3. Composite Films Made from Ceramic and Polymer Powders

The co-deposition of polymer and ceramic powders by PAD for the sake of obtaining films with mixed properties is so far only scarcely reported. In some of the existing studies, polymer was added to the ceramic base material to influence the dielectric properties of the PAD films.[28,62,121–124] Other works focused on biocompatible coatings for implant materials,[4] magnetic shielding films for near-field communication,[114,125]
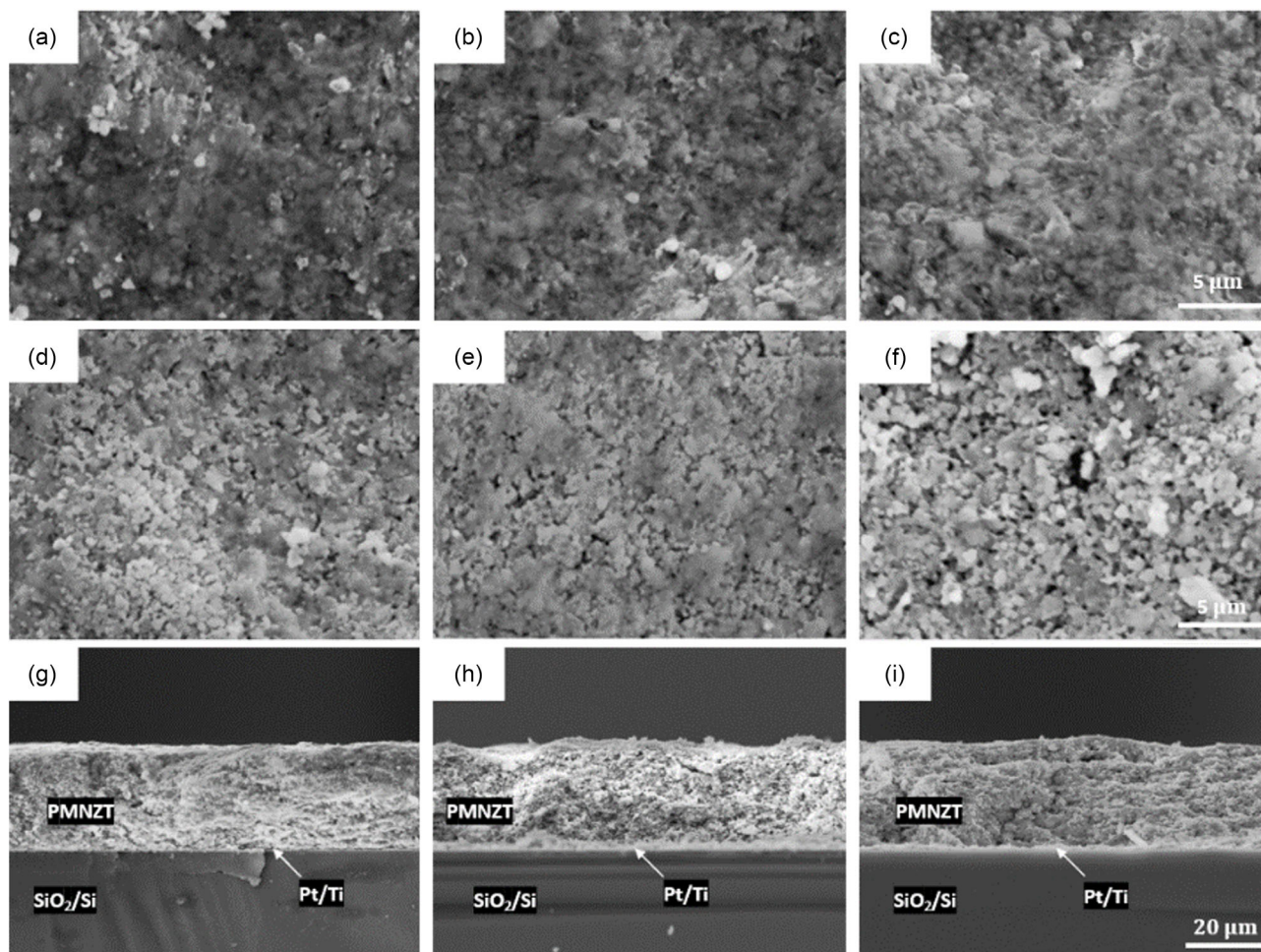

Figure 21. SEM images of the surface and cross-section morphology of PAD films obtained from mixtures of PMNZT and PVDF powders with different PVDF content deposited on platinized silicon substrates. Surface morphology of mixed PMNZT/PVDF films with varying PVDF content directly after PAD deposition: a) 3 wt%, b) 5 wt%, and c) 10 wt%, and after PAD heat treatment at 700 °C: d) 3 wt%, e) 5 wt%, and f) 10 wt%; cross sections of mixed PMNZT/PVDF films with varying PVDF content after PAD heat treatment at 700 °C: g) 3 wt%, h) 5 wt%, and i) 10 wt%. Adapted with permission.[118] Copyright 2009, Elsevier B.V.

hydrophobic and transparent glass coatings,[126,127] and porous thermal insulation coatings.[128]

These works reveal that the mechanism of simultaneous deposition of polymer and ceramic powders is significantly different to the deposition of pure ceramics. During aerosol generation, the concentration of polymer particles in the aerosol is increased compared to the concentration in the non-aerosolized powder because of the lower surface energy and specific density of the polymer particles compared to the ceramic particles. This results in preferential deposition of polymer particles early during the PAD process, and thus a nonuniform, less reproducible film quality.[127,129,130] To overcome this problem, Cho et al. and Kim et al. produced PCC powders for the PAD process. These powders were obtained by coating ceramic particles with a polymer layer, so that the two components could not separate during aerosolization.[127,130] To that end, Cho et al. dispersed $BaTiO_3$ powder particles in a solution of PVDF in acetone and stirred the dispersion for 72 h. After drying at room temperature, a 10–20 nm thick PVDF film was observed on the particles by TEM.[130] Kim et al. formed a $PTFE$–Al_2O_3 composite powders by first producing an Al_2O_3/polydimethylsiloxane (PDMS)/PTFE composite, which was then pyrolyzed. For this purpose, a PDMS oligomer was added as dispersing agent, together with a cross-linker. After mixing all components and subsequently heating the mixture at 80 °C for 20 min, a ductile cross-linked PDMS network was formed. The resulting Al_2O_3/PDMS/PTFE composite was annealed at 450 °C to partially pyrolyze the PDMS, which caused a ductile-to-brittle transition and yielded the Al_2O_3/PTFE composite powder.[127] In both studies, the deposition of the polymer-modified ceramic powders

was successful.[127,130] However, it could not be demonstrated that the thus obtained PAD films had a higher uniformity than films obtained by a simple manual mixture of the two components.

As discussed in a previous section, the ductility of polymer substrates results in shock absorption during the PAD process. This reduces the energy available for fracturing of the ceramic particles and thus alters the morphology of the films obtained. A similar effect was observed when polymer-containing powders were used. PAD films had an increased crystallite size after co-deposition of ceramic and polymer particles compared to deposition of the pure ceramic powders due to shock adsorption by the polymer component.[28,62,114,121–127] Also, the polymer to ceramics ratio in the composite powder changed the microstructure of the resulting films and caused an increase in the film roughness with increasing polymer concentration.[124,126,127,130] For example, Cho et al. deposited Al_2O_3–$PTFE$ composite powders with different concentrations of PTFE on glass substrates.[126] For these experiments, they mixed Al_2O_3 powder with a mean particle diameter of 0.4–0.5 µm with different amounts (0.01–1 wt%) of PTFE powder with 0.2 µm mean size. The composite powder was dried at 100 °C in a furnace for 24 h.[126] The film morphology changes observed by SEM and atomic force microscopy (AFM) are shown in **Figure 22**a–f. Both data sets indicate an increase in surface inhomogeneity and roughness (Figure 22a–f, right) with increasing polymer content. The SEM images show that up to 0.1 wt% PTFE, the obtained films were homogeneous but became increasingly rough compared to the pure alumina powder (Figure 22a–d, left). Starting at a concentration of 0.3 wt% PTFE, round craters with protrusions
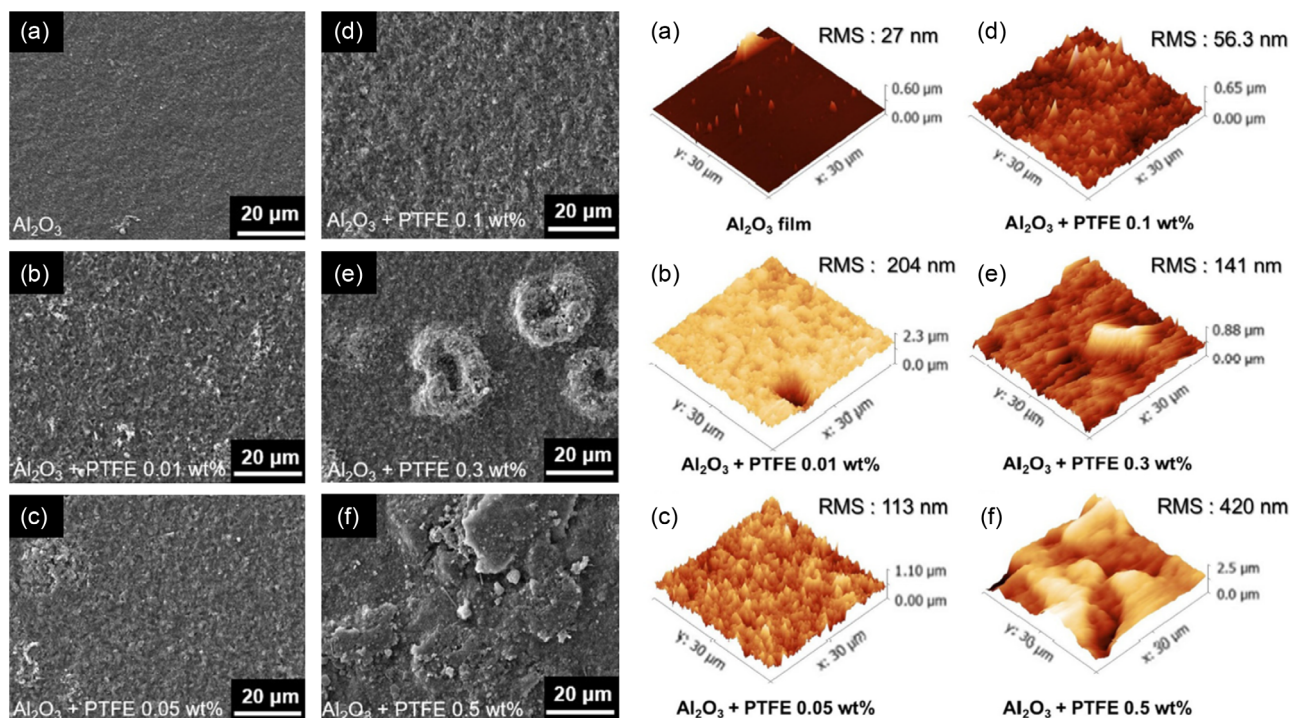

Figure 22. SEM and AFM images of the surface morphology of Al_2O_3–$PTFE$ composite coatings. SEM images (left) and AFM images (right) with average roughness values of a) Al_2O_3, b) Al_2O_3-0.01 wt%-PTFE, c) Al_2O_3-0.05 wt%-PTFE, d) Al_2O_3-0.1 wt%-PTFE, e) Al_2O_3-0.3 wt%-PTFE, and f) Al_2O_3-0.5 wt%-PTFE composite films deposited by PAD. Adapted with permission.[126] Copyright 2018, Elsevier Ltd. and Techna Group S.r.l.

appeared (Figure 22e, left), which were assigned to PTFE agglomerates using energy-dispersive X-ray spectroscopy (EDS). With a further increase in the PTFE content, the film partially peeled off (Figure 22f, left). The roughness profiles measured by AFM showed that the smoothest composite material was achieved at a moderate amount of 0.1 wt% PTFE (Figure 22d, right). The transmittance of the resulting films decreased with increasing PTFE content. The hydrophobicity reached a maximum at 0.2 wt% PTFE and sharply decreased with higher PTFE content. This was correlated to an increasing roughness.[126] The authors concluded that up to a certain percentage of polymer, the PTFE particles primarily fill up defects in the deposited Al_2O_3 composite film. They assumed that with a further increase of polymer content, the polymer particles agglomerate, which increasingly disrupts the deposition process.[126]

In addition to the earlier-described negative effects of co-deposition of ceramics and polymer particles on the surface homogeneity, beneficial effects have also been identified. In some papers, it was reported that the deposition rate for AcD of polymer–ceramic powders was up to 10 times higher than for the PAD of pure ceramic powders.[62,121,129] This can be useful for systems where a small amount of polymer does not change the desired overall properties, but an increase in the process efficiency is required. The authors of these works leave the reason for this observation undiscussed, but it is plausible to assume that the shock-absorption effect also reduces the abrasive effect of unsuitable particles in the aerosol. Additionally, it is possible that the higher ductility of polymeric particles leads to an improved anchor layer formation. In a very recent study, Yun et al. utilized agglomeration of $ZrSiO_2$ and polyethylene (PE) particles to adjust the kinetic energy of the deposited particles.[128] Without PE, the submicrometer-sized $ZrSiO_2$ powder formed a thick but nonuniform film with weak adhesion to the Al substrate. With PE, in contrast, a

relatively smooth, homogeneous film with uniform porosity could be deposited. The pore size (Figure 23a,b) increased with a higher amount of PE in film (determined via the carbon content in the film using EDS, Figure 23d,e).

The improved film formation compared to the pure ceramic powder was explained by the increased kinetic energy of the $ZrSiO_2$–PE agglomerates compared to the pure $ZrSiO_2$ particles.[128] However, as the adhesion of the composite films was too weak, the composite powders were additionally mixed with Y_2O_3 (Figure 23c,f). The adhesive strength of the Y_2O_3–$ZrSiO_2$–PE composite films measured according to ASTM C633-01 showed an increase to 37 MPa, compared to 15 MPa for the $ZrSiO_2$–PE composite films. This increase was associated with an increased hammering effect of the additionally introduced Y_2O_3 particles.[128]

Another important positive effect of polymer addition to PAD powders is the reduction of residual stresses in the deposited films, which is one of the main problems within the context of materials obtained by PAD.[10] Kim et al. indirectly demonstrated this feature by showing that the curvature of an Al_2O_3 green sheet was reduced when PAD-coated with an Al_2O_3–PI composite film, while this was not observed with a pure Al_2O_3 coating. The reduction of internal stresses of PAD films by AcD of polymer–ceramic powders was also confirmed by Kim et al. for Al_2O_3–PTFE composite coatings.[131]

One of the most important but so far largely unaddressed research questions in the context of PAD or AcD concerns the desired properties of polymer powders for successful PAD or AcD. In this context, Kwon et al. used two mechanically different polymers, PMMA and PI, and deposited them individually and as a mixture with Al_2O_3 particles.[129] SEM surface imaging of an Al_2O_3-15 wt%-PMMA film and a pure Al_2O_3 film demonstrated that the film morphology of the composite film was close to that of the pure ceramic film (Figure 24a,b). The Al_2O_3–PI composite
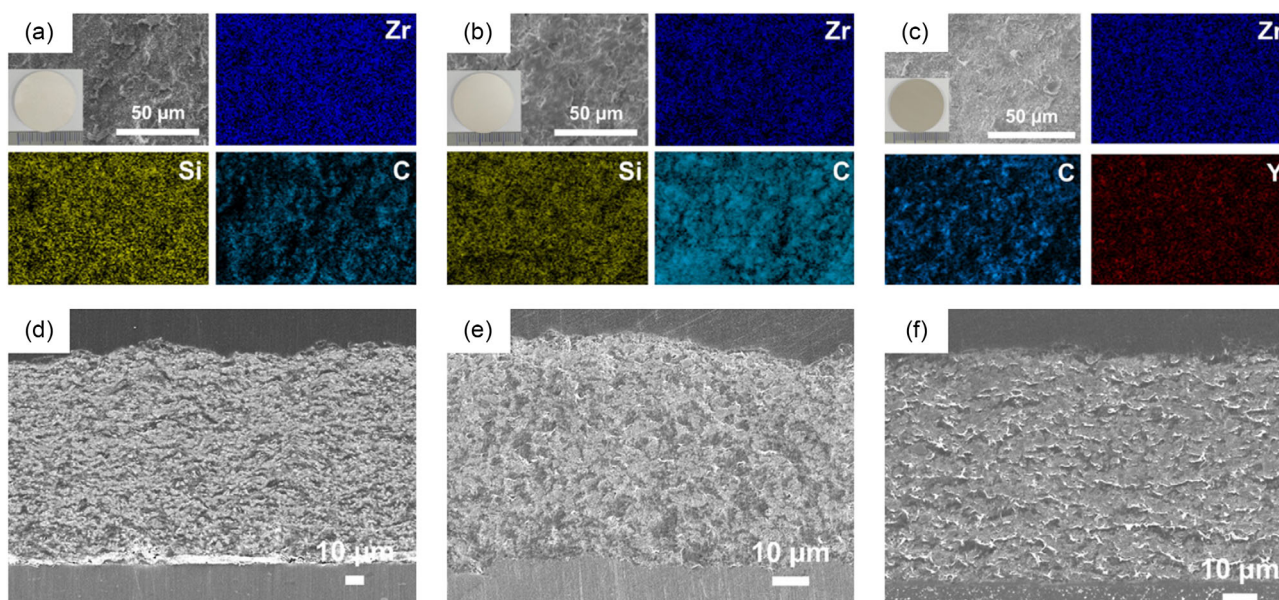

Figure 23. SEM surface morphology images, EDS maps, and SEM cross-section images of $ZrSiO_2$–PE and Y_2O_3–$ZrSiO_2$–PE composite coatings. SEM surface morphology images and EDS maps of a) $ZrSiO_2$-0.25 wt%-PE, b) $ZrSiO_2$-2 wt%-PE, and c) 30 wt%-Y_2O_3-70 wt%-$ZrSiO_2$-PE composite films deposited on aluminum substrates. Cross sections of d) $ZrSiO_2$-0.25 wt%-PE, e) $ZrSiO_2$-2 wt%-PE, and f) 30 wt%-Y_2O_3-70 wt%-$ZrSiO_2$-PE. Adapted with permission.[128] Copyright 2023, The Korean Ceramic Society.

**ADVANCED
SCIENCE NEWS**

www.advancedsciencenews.com

**ADVANCED
ENGINEERING
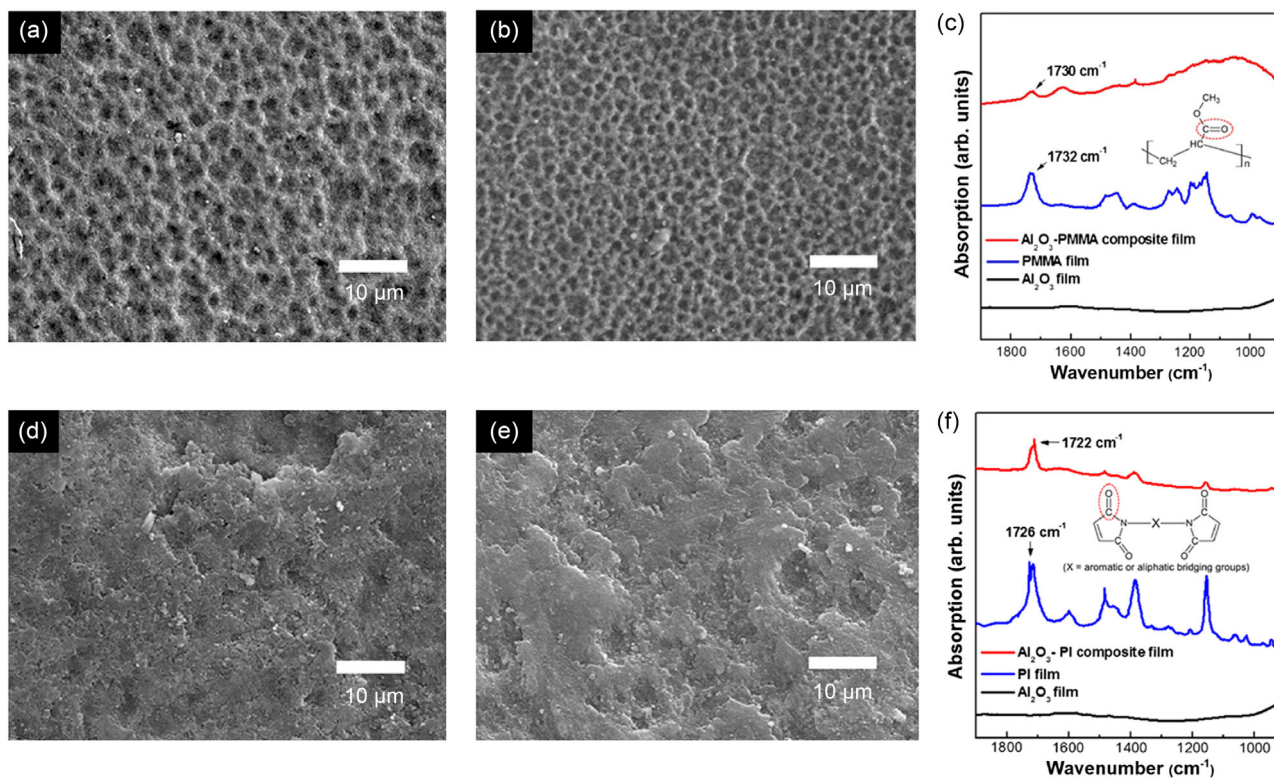MATERIALS**

www.aem-journal.com

Figure 24. SEM surface morphology images and infrared spectra of Al_2O_3–PMMA and Al_2O_3–PI composite films. SEM surface morphology images of PAD films made from a) Al_2O_3-15 wt%-PMMA, b) Al_2O_3, d) Al_2O_3-15 wt%-PI, and e) PI. FTIR spectra of c) Al_2O_3-15 wt%-PMMA and Al_2O_3 films compared to a pure PMMA film, and f) Al_2O_3-15 wt%-PI and PI films compared to a pure Al_2O_3 film. Adapted with permission.[129] Copyright 2012, Springer Nature.

film, in contrast, showed a microstructure similar to that of a pure PI film (Figure 24d,e). IR spectroscopy showed that the content of PMMA in the Al_2O_3–PMMA composite film was low (Figure 24c). In line with these observations, the hardness of the Al_2O_3–PMMA composite film was close to that of the pure Al_2O_3 film, while the Al_2O_3–PI composite film showed properties close to that of a pure PI film. The authors concluded that the deposition of two composite films occurred by different mechanisms related to the different mechanical properties of the polymer (**Figure 25**). The more ductile PMMA particles undergo strong plastic deformation on impact. The PI particles, in contrast, fracture like the ceramic particles. This fundamentally different mechanical behavior of the two polymers during deformation was also found when examining the polymer particles before and after processing in a ball mill.[129]

Although this is a first indication that polymer particles can fracture and deform plastically in PAD, analogously to ceramic particles, there is no systematic evidence of this behavior yet. It is known that a temperature- and strain-rate-dependent ductile-to-brittle transition also exists for a large number of polymers.[133] This was investigated for both semicrystalline and amorphous polymers.[134,135] In most cases, however, the experimental data only exist for quasistatic and intermediate strain rates. Shock data, which would be comparable with the conditions during AD, is rarely available.[136] One method often used to obtain information about the ductile-to-brittle response of polymers

under very high strain rates, the Taylor impact, consists of a slender rod of material that is impacted at high speed into an approximately rigid anvil.[137] Rae et al. used this method to demonstrate a ductile-to-brittle transition occurring at room temperature at an impact velocity of $134\,m\,s^{-1}$ for PTFE samples. This transition was associated with a pressure-induced phase transformation that occurs at around 0.65 GPa.[138] Since impact pressures are assumed to be significantly higher in the AD process[29,33,34] and PTFE is also a widely used polymer component in AcD,[114,121–123,125–127] it is reasonable to assume that such favorable transitions under high strain rates could be found for other possible polymer systems.

However, it should be noted that the Taylor impact is a measurement method for bulk materials, and that the strain rate occurring in that experiment could still be significantly below the conditions of the AD process. For these reasons, an exact investigation of the deformation behavior of polymer particles under conditions close to the AD process is essential for future work.

In summary, the so far published work described successful PAD co-deposition of polymer–ceramic combinations by which the functional properties of the two material classes are combined. In other cases, the application of polymers as a sacrificial phase enabled the production of porous ceramics. Positive effects of polymer addition included a better anchor layer formation on polymer substrates for some polymer–ceramic combinations, an
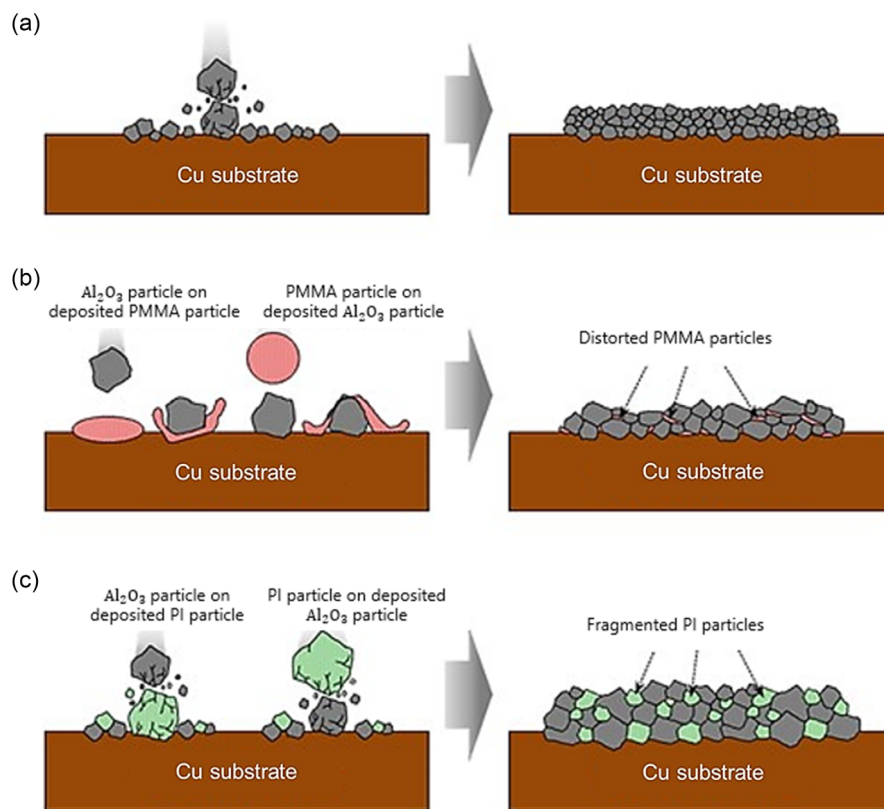
**ADVANCED
SCIENCE NEWS**
www.advancedsciencenews.com

**ADVANCED
ENGINEERING
MATERIALS**
www.aem-journal.com

Figure 25. Deposition mechanisms for composite powders of Al_2O_3 and two mechanically different polymers. a) Deposition mechanism for pure Al_2O_3. b) Deposition mechanism for Al_2O_3–PMMA composite powder via distortion of PMMA particles. c) Deposition mechanism for Al_2O_3–PI composite powder via fragmentation of PI particles. Adapted with permission.[129] Copyright 2012, Springer Nature.

increase in the deposition rate due to the shock-absorption effect, and a reduction of residual stresses in the deposited composite films. For other materials combinations, severe disadvantages were observed, including a reduced layer adhesion and a reduced coating homogeneity. Certain materials combinations were either not yet studied or not yet successfully deposited, e.g., polymer powders on top of polymer substrates or mixtures of polymer powders on any kind of substrate. The deposition of polymer powders on substrates of other material classes was also hardly investigated. The results for the deposition of PI films by PAD indicate that brittle polymers are particularly worthwhile to consider in more detail in future studies. Also, as some polymers are notoriously difficult to dissolve and thus cannot be coated by solution methods, PAD may provide an avenue to obtain coatings from these materials.

Another important topic that has been barely touched is the adaptation of PAD process parameters to the use of polymers. Is there a size-dependent deposition window for polymer particles, similar to that found for ceramics; and how can suitable polymer powders be produced in the most efficient way? Various methods are available for adjusting the particle size distribution of polymers in a very narrow range, such as emulsion polymerization,[139,140] spray drying,[141] and nanoprecipitation.[141–143] In conventional emulsion polymerization, droplets of a non-water-soluble monomer are dispersed in a continuous aqueous phase with the aid of a surfactant.[139] Parts of the hydrophobic

monomer migrates into micelles of a few nanometers in size formed by the surfactant, while a significantly larger part of the monomer remains as dispersed droplets of 1–10 μm size. If a water-soluble initiator is then added, monomer traces in the aqueous phase start forming oligomers and also migrate into the micelles, which serve as polymerization reactors so that polymer particles with a uniform size distribution are obtained.[139] For example, Liu et al. used emulsion polymerization with styrene as monomer, sodium dodecyl sulfate as surfactant, potassium persulfate (KPS) as initiator and a methanol–water mixture (20/80 w/w) as solvent to produce polystyrene nanoparticles (**Figure 26**a–d).[140] Similar results were achieved by Draheim et al. using nanospray drying and nanoprecipitation for poly (lactic-co-glycolic acid) (PLGA) nanoparticles.[141]

With nanoprecipitation, PLGA nanoparticles with an average particle size of 50–177 nm and a dispersity of 0.013–0.294 could be produced, while much larger particle sizes (2–163 μm) with a much higher dispersity close to 1 were obtained with nanospray drying.[141] One of the most detailed studies on the nanoprecipitation of various hydrophobic polymers was carried out by Hornig et al. who, in addition to the conventional dropping technique, where a polymer solution is dripped into a stirred nonsolvent, also investigated a variant using dialysis.[142] This had the advantage that, in addition to the formation of nanoparticles, low cmolar mass components of the dissolved polymers were also removed, but was significantly more time-consuming than
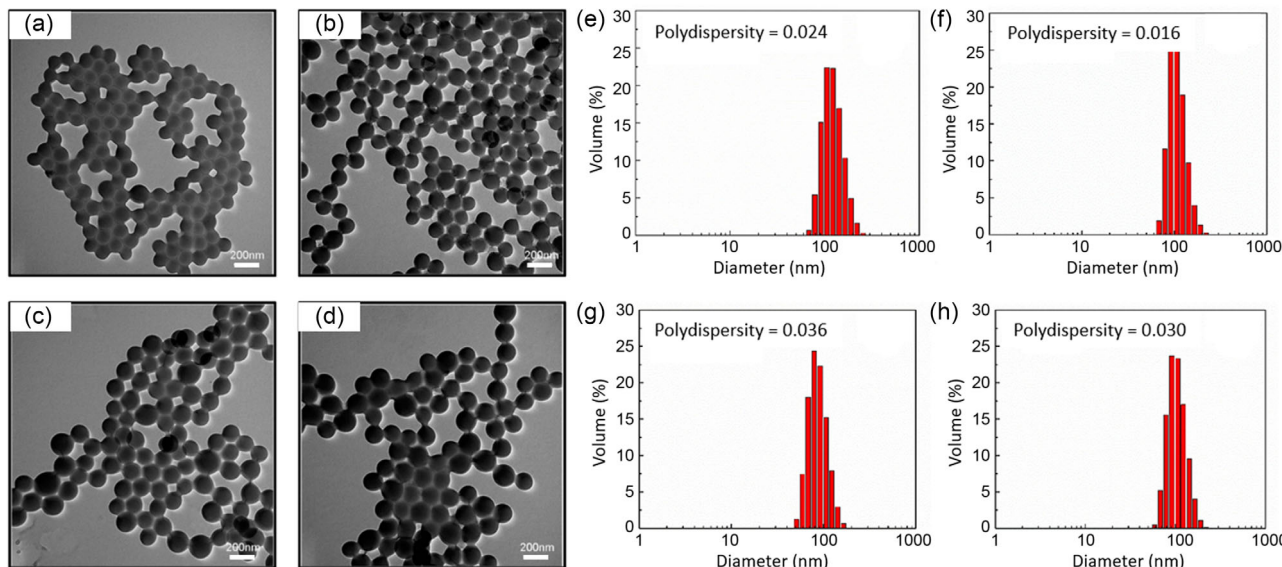
Figure 26. Particle morphology and size distribution of polystyrene particles prepared by emulsion polymerization. TEM images of polystyrene particles prepared by emulsion polymerization using different initiator concentrations of KPS: a) 0.3 wt%, b) 0.6 wt%, c) 0.9 wt%, and d) 1.2 wt%. e–h) Corresponding particle size distributions in the same order. Adapted with permission.[140] Copyright 2016, MDPI.

the dropping method.[143] In this way, a variety of polymers could be prepared in the form of precisely defined nanoparticles, including PS, PMMA, PC, poly(ε-caprolactone), poly(vinyl carbazole), poly(styrene-co-acrylic acid), and poly(vinyl acetate). PS and PMMA nanoparticles prepared by the dialysis method and the dropping method, respectively, are shown in **Figure 27**.[142] Average particle sizes were significantly larger for the dialysis method (200–700 nm) than for the dropping method (100–300 nm), while the dispersity values were similar for both methods (0.05–0.4).[142]

The work presented here clearly shows that polymer powders for the PAD process can be produced accurately over a wide range of particle sizes. If smaller particle sizes are needed, emulsion polymerization and nanoprecipitation are the methods of

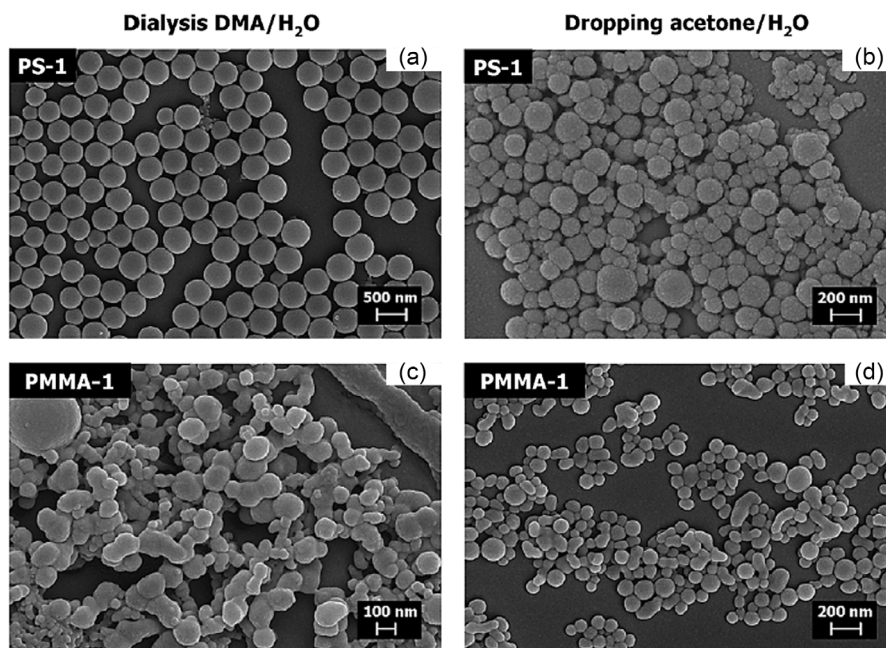**Figure 27.** Nanoparticles made by nanoprecipitation. SEM images of PS particles made by a) the dialysis method and b) the dropping method using dimethylacetamide (DMA) and acetone as the solvent, respectively. SEM images of PMMA particles made by c) the dialysis method and d) the dropping method using DMA and acetone as the solvent, respectively. Reproduced with permission.[142] Copyright 2009, Royal Society of Chemistry.

choice, while larger particles can be obtained by spray drying. The possibilities presented here for the production of defined polymer powders can be regarded as a basis for the systematic investigation of polymer powders within the PAD process and could lead to a deeper insight into the deposition mechanism of pure polymer and polymer composite powders via PAD.

4. Conclusion and Outlook

In the PAD process, fine ceramics particles with a size of 0.08–2 μm are accelerated through a nozzle to speeds of several hundred meters per second using a carrier gas. They then impact a substrate, where a part of their kinetic energy is converted into bonding energy by which bonds between the substrate and the particles and between different particles form. PAD takes place at room temperature within a quite narrow window of parameters that depend both on the materials used (density, particle size) and the processing setup (gas flow rate, particle velocity). PAD films form by fracturing and plastic deformation of the particles, which has been termed RTIC. The deposition mechanism is divided into two stages: the anchor layer formation, in which the plastic deformation of the substrate and the bonding to it occurs (Stage 1), and the film growth, in which the binding of the particles to each other and the densification of the film takes place (Stage 2). While many experimental studies dedicated to the deposition mechanism confirmed the RTIC mechanism propagated by Akedo et al. for different systems, there is yet no standardized binding theory for all materials, nor does it seem likely that all materials combinations will bind via the same mechanism. Future work in this area should thus focus on the anchor layer formation and clearly and quantitatively identify the conditions where such a layer is observed, and also investigate the bonding state at the interface of the PAD film and the substrate underneath, especially in those cases where no anchor layer is observed. The in silico studies treating the PAD mechanism confirm many of the experimental findings and add further details to the particle deposition and fracture mechanism.

The main parameters that influence the PAD process include the powder characteristics and pretreatment, the aerosol generation procedure and carrier gas type, the carrier gas flow rate and the nozzle type, as well as the substrate properties. It turns out that successful deposition involves a complex interplay between these parameters and future work must pay special attention to this aspect. The parameters that can be easily determined and adjusted, such as the particle size distribution, the crystallite size, as well as the surface roughness and hardness of the substrate, will be of particular importance here.

In research works that deal with the combination of ceramics and polymers in PAD processes, polymers were either used as substrates, as a sacrificial phase for the generation of porous structures, or as a dispersed phase in a composite film. It was demonstrated that various polymer–ceramic combinations can already be co-deposited by PAD, so that the functional properties of the two material classes are combined. In some of these systems, the addition of polymer improves the PAD process, for example, by enabling a better anchor layer formation on the substrate, an increase in the deposition rate due to the shock-absorption effect, or a reduction of residual stresses in the deposited films. In other cases, adverse effects such as reduced adhesion and increased film inhomogeneity were observed. The system parameters in which the benefits dominate over the disadvantages have yet to be determined by investigating a greater number of polymer–ceramic combinations, and by carefully characterizing the materials properties of these systems. Previous research already indicates that the relative toughness of the materials that are combined will play a role, but these effects must be quantified. Certain materials combinations have not yet been studied or successfully deposited at all, e.g., polymer powders on polymer substrates, or mixtures of polymer powders on any kind of substrate. This leaves ample space for researchers newly joining the field. In particular, it seems worthwhile to investigate the more brittle polymer systems. Another aspect that has not yet been studied is the deposition of polymers with incrementally changing chemical properties (e.g., copolymers with gradually changing composition). Systematic work on such systems could help elucidate the bonding mechanism between the PAD film and the substrate.

Another question is whether the PAD process parameters identified for the deposition of ceramic powders can be used in a similar way for the deposition of polymer or composite powders, or whether different particle size ranges or powder pretreatment procedures lead to better results. After all, ceramics are mostly polar materials, while many polymers are rather hydrophobic. It has yet to be determined if the differences in surface energy resulting from these properties affect the PAD process, or whether they are not significant in comparison to the high energies involved in the particle–substrate collisions. But even if that was the case, surface energies will affect particle agglomeration within the powder and thus could have an indirect effect on the PAD process. Answering these and other open questions will not only give access to new types of materials, but also provide a deeper insight into the deposition mechanism of polymer and composite powders via PAD.

Further, for a successful common future of polymers and the PAD process, the availability of suitable polymeric powders with sub-micron-particle size is crucial. While milling and grinding of polymers to obtain powders is possible, the obtained particle sizes are often too large. However, various other methods including emulsion polymerization, spray drying, and nanoprecipitation yield such particles and can be implemented for a large number of different polymers. Applications for PCC layers obtained by PAD beyond those already investigated include flexible sensor and microelectronics systems, membranes for the purification of gases and fluids, or mixed material multilayer systems such as battery systems. Such sinter-free PCCs layers can also be interesting to generate functional gradient materials or barrier coatings. All in all, it is our belief that there is hope for a common future for polymers and the PAD process—for sure in our own lab, and most likely also in PAD laboratories around the world.

ADVANCED
SCIENCE NEWS
www.advancedsciencenews.com

ADVANCED
ENGINEERING
MATERIALS
www.aem-journal.com

Conflict of Interest

The authors declare no conflict of interest.

Keywords

ceramics, coatings, composites, polymers, powder aerosol depositions, vacuum cold sprays, vacuum kinetic sprays

[1] J. Akedo, M. Lebedev, *Jpn. J. Appl. Phys.* **1999**, *38*, 5397.
[2] D. Hanft, J. Exner, M. Schubert, T. Stöcker, P. Fuierer, R. Moos, *J. Ceram. Sci. Technol.* **2015**, *6*, 147.
[3] D. W. Lee, H. J. Kim, Y. H. Kim, Y. H. Yun, S. M. Nam, *J. Am. Ceram. Soc.* **2011**, *94*, 3131.
[4] B.-D. Hahn, D.-S. Park, J.-J. Choi, J. Ryu, W.-H. Yoon, J.-H. Choi, H.-E. Kim, S.-G. Kim, *Surf. Coat. Technol.* **2011**, *205*, 3112.
[5] M. Y. Cho, S. Kim, I. S. Kim, E. S. Kim, Z. J. Wang, N. Y. Kim, S. W. Kim, J. M. Oh, *Adv. Funct. Mater.* **2020**, *30*, 2070017.
[6] Y. Imanaka, N. Hayashi, M. Takenouchi, J. Akedo, *J. Eur. Ceram. Soc.* **2007**, *27*, 2789.
[7] J. Iwasawa, R. Nishimizu, M. Tokita, M. Kiyohara, K. Uematsu, *J. Am. Ceram. Soc.* **2007**, *90*, 2327.
[8] T. Hoshina, T. Furuta, Y. Kigoshi, S. Hatta, N. Horiuchi, H. Takeda, T. Tsurumi, *Jpn. J. Appl. Phys.* **2010**, *49*, 09MC02.
[9] S. D. Johnson, E. R. Glaser, S.-F. Cheng, F. J. Kub, C. R. Eddy, *Appl. Phys. Express* **2014**, *7*, 035501.
[10] J. Adamczyk, P. Fuierer, *Surf. Coat. Technol.* **2018**, *350*, 542.
[11] M. Schubert, J. Exner, R. Moos, *Materials* **2014**, *7*, 5633.
[12] N. H. Khansur, U. Eckstein, K. Riess, A. Martin, J. Drnec, U. Deisinger, K. G. Webber, *Scr. Mater.* **2018**, *157*, 86.
[13] B. Daneshian, F. Gaertner, H. Assadi, D. Hoeche, W. Weber, T. Klassen, *J. Therm. Spray Technol.* **2021**, *30*, 503.
[14] M. Linz, F. Bühner, D. Paulus, L. Hennerici, Y. Guo, V. Mereacre, U. Mansfeld, M. Seipenbusch, J. Kita, R. Moos, *Adv. Mater.* **2023**, *36*, 2308294.
[15] Y. Furuya, S. Konuma, M. Hasegawa, *Surf. Coat. Technol.* **2023**, *458*, 129362.
[16] S. Lee, J. H. Park, C. G. Park, D.-Y. Jeong, N. M. Hwang, *Cryst. Growth Des.* **2021**, *21*, 7240.
[17] S. Choi, J.-H. Lim, E.-Y. Kang, H. Kim, Y.-M. Kong, D.-Y. Jeong, *J. Asian Ceram. Soc.* **2021**, *9*, 1128.
[18] N. Leupold, S. Denneler, G. Rieger, R. Moos, *J. Therm. Spray Technol.* **2021**, *30*, 480.
[19] P. Glosse, S. Denneler, O. Stier, R. Moos, *Materials* **2021**, *14*, 2502.
[20] Y. Matsubayashi, J. Akedo, *Ceram. Int.* **2023**, *49*, 21570.
[21] M. Linz, J. Exner, T. Nazarenus, J. Kita, R. Moos, *Open Ceram.* **2022**, *10*, 100253.
[22] Y. Akedo, E. Kubota, M. Shahien, M. Suzuki, J. Akedo, T. Fujino, K. Shinoda, *Plasma Chem. Plasma Process.* **2023**, *44*, 583.
[23] S. Biberger, N. Leupold, C. Witt, C. Greve, P. Markus, P. Ramming, D. Lukas, K. Schötz, F.-J. Kahle, C. Zhu, *Sol. RRL* **2023**, *7*, 2300261.
[24] R. Werner, J. S. Matejka, D. Schönauer-Kamin, R. Moos, *Energy Technol.* **2022**, *10*, 2101091.
[25] M. Sadl, U. Tomc, H. Ursic, *Materials* **2021**, *14*, 4548.
[26] J. J. Choi, J. H. Jang, D. S. Park, B. D. Hahn, W. H. Yoon, C. Park, *Solid State Phenom.* **2007**, *124*, 169.
[27] J.-H. Park, J. Akedo, M. Nakada, *Jpn. J. Appl. Phys.* **2006**, *45*, 7512.
[28] H. Kim, Y. Yoon, J. Kim, S. Nam, *Mater. Sci. Eng., B* **2009**, *161*, 104.
[29] J. Akedo, *J. Therm. Spray Technol.* **2008**, *17*, 181.
[30] M. Schubert, D. Hanft, T. Nazarenus, J. Exner, M. Schubert, P. Nieke, P. Glosse, N. Leupold, J. Kita, R. Moos, *Funct. Mater. Lett.* **2019**, *12*, 1930005.
[31] M. Schubert, M. Hahn, J. Exner, J. Kita, R. Moos, *Funct. Mater. Lett.* **2017**, *10*, 1750045.
[32] M. J. Mayo, *Int. Mater. Rev.* **1996**, *41*, 85.
[33] J. Akedo, *J. Am. Ceram. Soc.* **2006**, *89*, 1834.
[34] J. Akedo, *J. Ceram. Soc. Jpn.* **2020**, *128*, 101.
[35] K. Naoe, M. Nishiki, A. Yumoto, *J. Therm. Spray Technol.* **2013**, *22*, 1267.
[36] J. Kwon, H. Park, I. Lee, C. Lee, *Surf. Coat. Technol.* **2014**, *259*, 585.
[37] T. P. Mishra, R. Singh, R. Mücke, J. Malzbender, M. Bram, O. Guillon, R. Vaßen, *J. Therm. Spray Technol.* **2021**, *30*, 488.
[38] D.-M. Chun, S.-H. Ahn, *Acta Mater.* **2011**, *59*, 2693.
[39] H. Park, J. Kwon, I. Lee, C. Lee, *Scr. Mater.* **2015**, *100*, 44.
[40] M. A. Piechowiak, J. Henon, O. Durand-Panteix, G. Etchegoyen, V. Coudert, P. Marchet, F. Rossignol, *J. Eur. Ceram. Soc.* **2014**, *34*, 1063.
[41] C. Lee, M.-Y. Cho, M. Kim, J. Jang, Y. Oh, K. Oh, S. Kim, B. Park, B. Kim, S.-M. Koo, *Sci. Rep.* **2019**, *9*, 2166.
[42] T. Shibuya, T. Mizuno, A. Iuchi, M. Hasegawa, *Mater. Trans.* **2020**, *61*, 540.
[43] J.-M. Oh, S.-M. Nam, *Jpn. J. Appl. Phys.* **2009**, *48*, 09KA07.
[44] D.-W. Lee, H.-J. Kim, Y.-N. Kim, M.-S. Jeon, S.-M. Nam, *Surf. Coat. Technol.* **2012**, *209*, 160.
[45] K. Naoe, M. Nishiki, K. Sato, *J. Therm. Spray Technol.* **2014**, *23*, 1333.
[46] J. Kim, J. I. Lee, D. S. Park, E. S. Park, *J. Appl. Phys.* **2015**, *117*, 014903.
[47] Y. Liu, Y. Wang, X. Suo, Y. Gong, C.-J. Li, H. Li, *Ceram. Int.* **2016**, *42*, 1640.
[48] L.-S. Wang, H.-F. Zhou, K.-J. Zhang, Y.-Y. Wang, C.-X. Li, X.-T. Luo, G.-J. Yang, C.-J. Li, *Ceram. Int.* **2017**, *43*, 4390.
[49] N. H. Khansur, U. Eckstein, Y. Li, D. A. Hall, J. Kaschta, K. G. Webber, *J. Am. Ceram. Soc.* **2019**, *102*, 5763.
[50] W. K. Tan, Y. Shigeta, A. Yokoi, G. Kawamura, A. Matsuda, H. Muto, *Appl. Surf. Sci.* **2019**, *483*, 212.
[51] H. Park, H. Kwon, J. Kim, C. Lee, *J. Therm. Spray Technol.* **2021**, *30*, 558.
[52] P. Baláž, M. Achimovičová, M. Baláž, P. Billik, Z. Cherkezova-Zheleva, J. M. Criado, F. Delogu, E. Dutková, E. Gaffet, F. J. Gotor, *Chem. Soc. Rev.* **2013**, *42*, 7571.
[53] F. Delogu, *J. Phys. Chem. B* **2011**, *115*, 21230.
[54] J. Dickinson, L. Jensen, A. Jahan-Latibari, *J. Vac. Sci. Technol., A* **1984**, *2*, 1112.
[55] L. Scudiero, J. Dickinson, Y. Enomoto, *Phys. Chem. Miner.* **1998**, *25*, 566.
[56] J. Akedo, M. Lebedev, *Jpn. J. Appl. Phys.* **2001**, *40*, 5528.
[57] M. Lebedev, J. Akedo, *Jpn. J. Appl. Phys.* **2002**, *41*, 6669.
[58] K. Mihara, T. Hoshina, H. Takeda, T. Tsurumi, *J. Ceram. Soc. Jpn.* **2009**, *117*, 868.
[59] K. Mihara, T. Hoshina, H. Kakemoto, H. Takeda, T. Tsurumi, *Key Eng. Mater.* **2010**, *421*, 165.
[60] D.-W. Lee, H.-J. Kim, S.-M. Nam, *J. Korean Phys. Soc.* **2010**, *57*, 1115.
[61] E. Fuchita, E. Tokizaki, Y. Sakka, *J. Ceram. Soc. Jpn.* **2010**, *118*, 767.
[62] H.-J. Kim, S.-M. Nam, *Electron. Mater. Lett.* **2012**, *8*, 65.
[63] K. Naoe, K. Sato, M. Nishiki, *J. Ceram. Soc. Jpn.* **2014**, *122*, 110.
[64] Z. Yao, C. Wang, Y. Li, H.-K. Kim, N.-Y. Kim, *Nanoscale Res. Lett.* **2014**, *9*, 435.
[65] J. Exner, M. Hahn, M. Schubert, D. Hanft, P. Fuierer, R. Moos, *Adv. Powder Technol.* **2015**, *26*, 1143.
[66] J. Exner, M. Schubert, D. Hanft, J. Kita, R. Moos, *J. Eur. Ceram. Soc.* **2019**, *39*, 592.
[67] D. Hanft, M. Bektas, R. Moos, *Materials* **2018**, *11*, 1342.

**ADVANCED
SCIENCE NEWS**

www.advancedsciencenews.com

**ADVANCED
ENGINEERING
MATERIALS**

www.aem-journal.com

[68] D. Hanft, P. Glosse, S. Denneler, T. Berthold, M. Oomen, S. Kauffmann-Weiss, F. Weis, W. Häßler, B. Holzapfel, R. Moos, *Materials* **2018**, *11*, 1572.

[69] S. Baba, J. Akedo, M. Tsukamoto, N. Abe, *J. Am. Ceram. Soc.* **2006**, *89*, 1736.

[70] G.-J. Yang, C.-J. Li, K.-X. Liao, X.-L. He, S. Li, S.-Q. Fan, *Thin Solid Films* **2011**, *519*, 4709.

[71] F. Cao, H. Park, J. Heo, J. Kwon, C. Lee, *J. Therm. Spray Technol.* **2013**, *22*, 1109.

[72] T. Maki, S. Sugimoto, T. Kagotani, K. Inomata, J. Akedo, T. Ishikawa, K. Ohmori, *J. Alloys Compd.* **2006**, *408*, 1409.

[73] M. Lebedev, J. Akedo, T. Ito, *J. Cryst. Growth* **2005**, *275*, e1301.

[74] C.-W. Kim, J.-H. Choi, H.-J. Kim, D.-W. Lee, C.-Y. Hyun, S.-M. Nam, *Ceram. Int.* **2012**, *38*, 5621.

[75] S. Ghosh, X. Chen, C. Li, B. A. Olson, C. J. Hogan Jr, *AIChE J.* **2020**, *66*, e16874.

[76] G. Song, J. Adamczyk, Y. Park, E. S. Toberer, C. J. Hogan Jr, *Adv. Eng. Mater.* **2021**, *23*, 2100255.

[77] H. Kwon, Y. Kim, H. Park, C. Lee, *J. Therm. Spray Technol.* **2021**, *30*, 542.

[78] J. Exner, M. Linz, J. Kita, R. Moos, *Int. J. Appl. Ceram. Technol.* **2021**, *18*, 2178.

[79] M. Lee, J. Park, D. Kim, S. Yoon, H. Y. Kim, D. Kim, S. James, S. Chandra, T. Coyle, J. Ryu, *J. Aerosol Sci.* **2011**, *42*, 771.

[80] S. G. Bierschenk, M. F. Becker, D. Kovar, *J. Aerosol Sci.* **2023**, *169*, 106113.

[81] T. Goto, Y. Matsubayashi, J. Akedo, *Ceram. Int.* **2024**, *50*, 892.

[82] H. Bae, J. Choi, G. M. Choi, *Solid State Ionics* **2013**, *236*, 16.

[83] H. Katanoda, K. Matsuo, *Mater. Trans.* **2006**, *47*, 1620.

[84] H. Park, J. Kim, C. Lee, *Scr. Mater.* **2015**, *108*, 72.

[85] H. Park, J. Kim, S. B. Lee, C. Lee, *J. Therm. Spray Technol.* **2017**, *26*, 327.

[86] H. Park, H. Kwon, C. Lee, *J. Therm. Spray Technol.* **2017**, *26*, 1616.

[87] S. D. Johnson, D. Schwer, D.-S. Park, Y.-S. Park, E. P. Gorzkowski, *Surf. Coat. Technol.* **2017**, *332*, 542.

[88] C. Li, N. Singh, A. Andrews, B. A. Olson, T. E. Schwartzentruber, C. J. Hogan Jr, *Int. J. Heat Mass Transfer* **2019**, *129*, 1161.

[89] A. Z. Yeganeh, M. Jadidi, C. Moreau, A. Dolatabadi, *Surf. Coat. Technol.* **2019**, *370*, 269.

[90] H. Park, H. Kwon, Y. Kim, C. Lee, *J. Therm. Spray Technol.* **2019**, *28*, 1945.

[91] K. S. Kim, K. A. Lee, *J. Am. Ceram. Soc.* **2020**, *103*, 54.

[92] H. Kwon, Y. Kim, J. Kim, H. Seok, D. Kim, C. Lee, *Surf. Coat. Technol.* **2020**, *394*, 125866.

[93] R. Saunders, S. D. Johnson, D. Schwer, E. A. Patterson, H. Ryou, E. P. Gorzkowski, *J. Therm. Spray Technol.* **2021**, *30*, 523.

[94] H. Ogawa, *Mater. Trans.* **2005**, *46*, 1235.

[95] H. Ogawa, *Mater. Trans.* **2006**, *47*, 1945.

[96] H. Ogawa, *Mater. Trans.* **2007**, *48*, 2067.

[97] B. Daneshian, H. Assadi, *J. Therm. Spray Technol.* **2014**, *23*, 541.

[98] H. Jami, A. Jabbarzadeh, *Surf. Coat. Technol.* **2020**, *382*, 125173.

[99] B. Daneshian, F. Gärtner, H. Assadi, M. V. Vidaller, D. Höche, T. Klassen, *Surf. Coat. Technol.* **2022**, *429*, 127886.

[100] G. Song, H. Yang, C. J. Hogan Jr, *Appl. Surf. Sci.* **2022**, *585*, 152603.

[101] G. Song, C. J. Hogan Jr, *Int. J. Plast.* **2023**, *170*, 103758.

[102] G. Song, J. M. Adamczyk, E. S. Toberer, C. J. Hogan Jr, *Appl. Surf. Sci.* **2023**, *609*, 155245.

[103] S. Kuroyanagi, K. Shinoda, A. Yumoto, J. Akedo, *Acta Mater.* **2020**, *195*, 588.

[104] E. Munch, M. E. Launey, D. H. Alsem, E. Saiz, A. P. Tomsia, R. O. Ritchie, *Science* **2008**, *322*, 1516.

[105] M. A. Meyers, P.-Y. Chen, A. Y.-M. Lin, Y. Seki, *Prog. Mater. Sci.* **2008**, *53*, 1.

[106] X. Wang, M. Jiang, Z. Zhou, J. Gou, D. Hui, *Composites, Part B* **2017**, *110*, 442.

[107] P. Judeinstein, C. Sanchez, *J. Mater. Chem.* **1996**, *6*, 511.

[108] M. García, J. Marchese, N. Ochoa, *J. Appl. Polym. Sci.* **2010**, *118*, 2417.

[109] Y. Zare, *Composites, Part A* **2016**, *84*, 158.

[110] D. Chun, M. Kim, J. Lee, S. Ahn, *CIRP Ann.* **2008**, *57*, 551.

[111] J. Ryu, K. Y. Kim, J. J. Choi, B. D. Hahn, W. H. Yoon, B. K. Lee, D. S. Park, D. Y. Jeong, C. Park, *J. Am. Ceram. Soc.* **2009**, *92*, 524.

[112] H. Kim, S. Park, Y. Park, D. Choi, B. Yoo, C. S. Lee, *Sens. Actuators, B* **2018**, *274*, 331.

[113] A. Kitajima, M. Tsukamoto, J. Akedo, *J. Ceram. Soc. Jpn.* **2010**, *118*, 417.

[114] H.-J. Kim, S.-M. Nam, J.-H. Koh, *J. Nanosci. Nanotechnol.* **2014**, *14*, 7915.

[115] M. N. E. A. Al Nasim, D.-M. Chun, *Surf. Coat. Technol.* **2017**, *309*, 172.

[116] R. Calvo, P. Fuierer, *Int. J. Appl. Ceram. Technol.* **2023**, *20*, 395.

[117] S.-Q. Fan, C.-J. Li, C.-X. Li, G.-J. Liu, G.-J. Yang, L.-Z. Zhang, *Mater. Trans.* **2006**, *47*, 1703.

[118] J.-J. Choi, B.-D. Hahn, J. Ryu, W.-H. Yoon, B.-K. Lee, D.-S. Park, *Sens. Actuators, A* **2009**, *153*, 89.

[119] J.-J. Choi, J.-H. Choi, J. Ryu, B.-D. Hahn, J.-W. Kim, C.-W. Ahn, W.-H. Yoon, D.-S. Park, *J. Alloys Compd.* **2012**, *545*, 186.

[120] G. Han, J. Ryu, W. H. Yoon, J. J. Choi, B. D. Hahn, D. S. Park, *J. Am. Ceram. Soc.* **2011**, *94*, 1509.

[121] H.-J. Kim, Y.-H. Kim, S.-M. Nam, Y. J. Yoon, J.-H. Kim, *J. Korean Phys. Soc.* **2010**, *57*, 1086.

[122] Y.-H. Kim, H.-J. Kim, J.-H. Koh, J.-G. Ha, Y.-H. Yun, S.-M. Nam, *Ceram. Int.* **2011**, *37*, 1859.

[123] S. H. Cho, Y. J. Yoon, H. T. Kim, J. Kim, H.-J. Kim, S. M. Nam, H. K. Baik, J.-H. Kim, *Ceram. Int.* **2012**, *38*, S131.

[124] H.-J. Kim, S.-M. Nam, *Nanoscale Res. Lett.* **2012**, *7*, 92.

[125] H.-J. Kim, O.-Y. Kwon, C.-I. Jang, T. K. Kim, J. R. Oh, Y. J. Yoon, J.-H. Kim, S.-M. Nam, J.-H. Koh, *Electron. Mater. Lett.* **2013**, *9*, 805.

[126] M.-Y. Cho, S.-J. Park, S.-M. Kim, D.-W. Lee, H.-K. Kim, S.-M. Koo, K.-S. Moon, J.-M. Oh, *Ceram. Int.* **2018**, *44*, 16548.

[127] I. S. Kim, M. Y. Cho, Y. Jeong, Y. C. Shin, D. W. Lee, C. Park, S. M. Koo, W. Ho Shin, W. J. Yang, Y. Park, *J. Am. Ceram. Soc.* **2021**, *104*, 1716.

[128] S.-J. Yun, J.-H. Kim, H.-A. Cha, C.-W. Ahn, Y. K. Moon, J. Jang, W.-H. Yoon, J.-J. Choi, B.-D. Hahn, *J. Korean Ceram. Soc.* **2023**, *61*, 142.

[129] O.-Y. Kwon, H.-J. Na, H.-J. Kim, D.-W. Lee, S.-M. Nam, *Nanoscale Res. Lett.* **2012**, *7*, 261.

[130] S. H. Cho, Y. J. Yoon, *J. Korean Phys. Soc.* **2016**, *68*, 340.

[131] H.-J. Kim, Y.-H. Kim, J.-W. Lee, S.-M. Nam, Y. J. Yoon, J.-H. Kim, *J. Nanoelectron. Optoelectron.* **2012**, *7*, 287.

[132] R. K. Nishihora, P. L. Rachadel, M. G. N. Quadri, D. Hotza, *J. Eur. Ceram. Soc.* **2018**, *38*, 988.

[133] B. Jang, D. Uhlmann, J. V. Sande, *J. Appl. Polym. Sci.* **1984**, *29*, 3409.

[134] S. J. Hocker, W. T. Kim, H. C. Schniepp, D. E. Kranbuehl, *Polymer* **2018**, *158*, 72.

[135] J. Liu, Z. Zhao, W. Wang, J. W. Mays, S. Q. Wang, *J. Polym. Sci., Part B: Polym. Phys.* **2019**, *57*, 758.

[136] N. K. Bourne, *J. Dyn. Behav. Mater.* **2016**, *2*, 33.

[137] C. R. Siviour, presented at *AIP Conf. Proc.* **2017**, *1793*, 060029.

[138] P. J. Rae, G. T. Gray, D. M. Dattelbaum, N. K. Bourne, presented at *AIP Conf. Proc.* **2004**, *706*, 671.

[139] C. Chern, *Prog. Polym. Sci.* **2006**, *31*, 443.

[140] B. Liu, Y. Wang, M. Zhang, H. Zhang, *Polymers* **2016**, *8*, 55.

[141] C. Draheim, F. De Crécy, S. Hansen, E.-M. Collnot, C.-M. Lehr, *Pharm. Res.* **2015**, *32*, 2609.

[142] S. Hornig, T. Heinze, C. R. Becer, U. S. Schubert, *J. Mater. Chem.* **2009**, *19*, 3838.

[143] S. Schubert, J. T. Delaney Jr, U. S. Schubert, *Soft Matter* **2011**, *7*, 1581.

**ADVANCED
SCIENCE NEWS**

www.advancedsciencenews.com

**ADVANCED
ENGINEERING
MATERIALS**

www.aem-journal.com

Marc Christopher Thiel studied materials science and engineering at Saarland University in Saarbrücken, Germany, and received his M.Sc. with a specialization in fracture mechanics in 2022. He then joined the group of Karen Lienkamp at the Chair of Polymer Materials at Saarland University. He is currently working on his Ph.D. thesis with focus on polymer–ceramic composites made by powder aerosol deposition.

Karen Lienkamp studied chemistry at Cambridge, UK, and Berlin, Germany. She obtained a Ph.D. in physical chemistry from the Johannes-Gutenberg-Universität in Mainz, Germany. She worked at the Max Plank-Institute for Polymer Research in Mainz, Germany, at the Department of Polymer Science and Engineering of the University of Massachusetts Amherst, MA, USA, and at the Institute of Microsystems Engineering of the Albert-Ludwigs-Universität in Freiburg, Germany. Since 2021, Prof. Lienkamp holds the Chair of Polymer Materials at the Department of Materials Science and Engineering at Saarland University. Her research interests include polymer coatings, polymer composites, and 3D-printed polymer materials.

2400503 (30 of 30)